3-27-2013

Evolution of dike opening during the March 2011 Kamoamoa fissure eruption, Kīlauea Volcano, Hawai'i

Paul Lundgren
California Institute of Technology

Michael Poland
Hawaiian Volcano Observatory, U.S. Geological Survey

Asta Miklius
Hawaiian Volcano Observatory, U.S. Geological Survey

Tim Orr
Hawaiian Volcano Observatory, U.S. Geological Survey

Sang-Ho Yun
California Institute of Technology

See next page for additional authors

Recommended Citation

Lundgren, P., et al. (2013), Evolution of dike opening during the March 2011 Kamoamoa fissure eruption, Kīlauea Volcano, Hawai'i. *Journal of Geophysical Research: Solid Earth, 118*, 897–914. DOI: 10.1002/jgrb.50108

Evolution of dike opening during the March 2011 Kamoamoa fissure eruption, Kīlauea Volcano, Hawai`i

Paul Lundgren,[1] Michael Poland,[2] Asta Miklius,[2] Tim Orr,[2] Sang-Ho Yun,[1] Eric Fielding,[1] Zhen Liu,[1] Akiko Tanaka,[3] Walter Szeliga,[4] Scott Hensley,[1] and Susan Owen[1]

Received 10 July 2012; revised 18 January 2013; accepted 24 January 2013; published 27 March 2013.

[1] The 5–9 March 2011 Kamoamoa fissure eruption along the east rift zone of Kīlauea Volcano, Hawai`i, followed months of pronounced inflation at Kīlauea summit. We examine dike opening during and after the eruption using a comprehensive interferometric synthetic aperture radar (InSAR) data set in combination with continuous GPS data. We solve for distributed dike displacements using a whole Kīlauea model with dilating rift zones and possibly a deep décollement. Modeled surface dike opening increased from nearly 1.5 m to over 2.8 m from the first day to the end of the eruption, in agreement with field observations of surface fracturing. Surface dike opening ceased following the eruption, but subsurface opening in the dike continued into May 2011. Dike volumes increased from 15, to 16, to 21 million cubic meters (MCM) after the first day, eruption end, and 2 months following, respectively. Dike shape is distinctive, with a main limb plunging from the surface to 2–3 km depth in the up-rift direction toward Kīlauea's summit, and a lesser projection extending in the down-rift direction toward Pu`u `Ō`ō at 2 km depth. Volume losses beneath Kīlauea summit (1.7 MCM) and Pu`u `Ō`ō (5.6 MCM) crater, relative to dike plus erupted volume (18.3 MCM), yield a dike to source volume ratio of 2.5 that is in the range expected for compressible magma without requiring additional sources. Inflation of Kīlauea's summit in the months before the March 2011 eruption suggests that the Kamoamoa eruption resulted from overpressure of the volcano's magmatic system.

Citation: Lundgren, P., M. Poland, A. Miklius, T. Orr, S.-H. Yun, E. Fielding, Z. Liu, A. Tanaka, W. Szeliga, S. Hensley, and S. Owen (2013), Evolution of dike opening during the March 2011 Kamoamoa fissure eruption, Kīlauea Volcano, Hawai`i, *J. Geophys. Res. Solid Earth*, *118*, 897–914, doi:10.1002/jgrb.50108.

1. Introduction

[2] Over the past several decades, geodetic data from Kīlauea Volcano, Hawai`i (Figure 1), have been used to explore dike emplacement processes through models for dike geometry, propagation, transient post-diking deformation, and interaction with the deep décollement fault that underlies the volcano and is associated with flank instability [*Cayol et al.*, 2000; *Owen et al.*, 2000a; *Segall et al.*, 2001; *Cervelli et al.*, 2002; *Desmarais and Segall*, 2007; *Montgomery-Brown et al.*, 2010, 2011]. Kīlauea's volcanism arises from magma channeled from depth through a central conduit system that feeds the southwest rift zone (SWRZ) and east rift zone (ERZ) at depths shallower than 10 km through lateral dikes [*Ryan*, 1988], possibly confined to a molten core at 3–5 km depth within the ERZ [*Johnson*, 1995]. Magma enters the rift zones as their deeper portions (>3 km) experience dilatant opening in response to magma injection and south flank sliding over a sub-horizontal décollement [*Dieterich*, 1988; *Delaney et al.*, 1990; *Owen et al.*, 1995, 2000a; *Morgan et al.*, 2000]. Diking events are one of the end results of the magmatic-structural system with dike intrusions having been interpreted as either passive [*Owen et al.*, 2000b; *Cervelli et al.*, 2002] or active [*Montgomery-Brown et al.*, 2010], based on whether there was significant pre-eruptive inflation of Kīlauea's summit (hereafter referred to as "the summit").

[3] Interferometric synthetic aperture radar (InSAR) data have provided increased resolution of dike complexity through detailed spatial sampling near the dike that is often difficult to achieve with more sparse in situ data [*Lundgren and Rosen*, 2003; *Wright et al.*, 2006; *Yun et al.*, 2006; *Montgomery-Brown et al.*, 2010; *Pallister et al.*, 2010]. Prior dike models constrained by InSAR data have generally been limited in their temporal resolution due to the sparse temporal sampling (approximately monthly) that has characterized most radar satellite missions. Studies of dike

[1]Jet Propulsion Laboratory, California Institute of Technology, Pasadena, California, USA.
[2]Hawaiian Volcano Observatory, U.S. Geological Survey, Hawaiian Volcanoes National Park, Hawaii, USA.
[3]Geological Survey of Japan, AIST, Tsukuba, Japan.
[4]Department of Geological Sciences, Central Washington University, Ellensburg, Washington, USA.

Corresponding author: P. Lundgren, Jet Propulsion Laboratory, California Institute of Technology 4800 Oak Grove Drive, MS 300-233, Pasadena, CA 91109-8099, USA. (Paul.R.Lundgren@jpl.nasa.gov)

2169-9313/13/10.1002/jgrb.50108

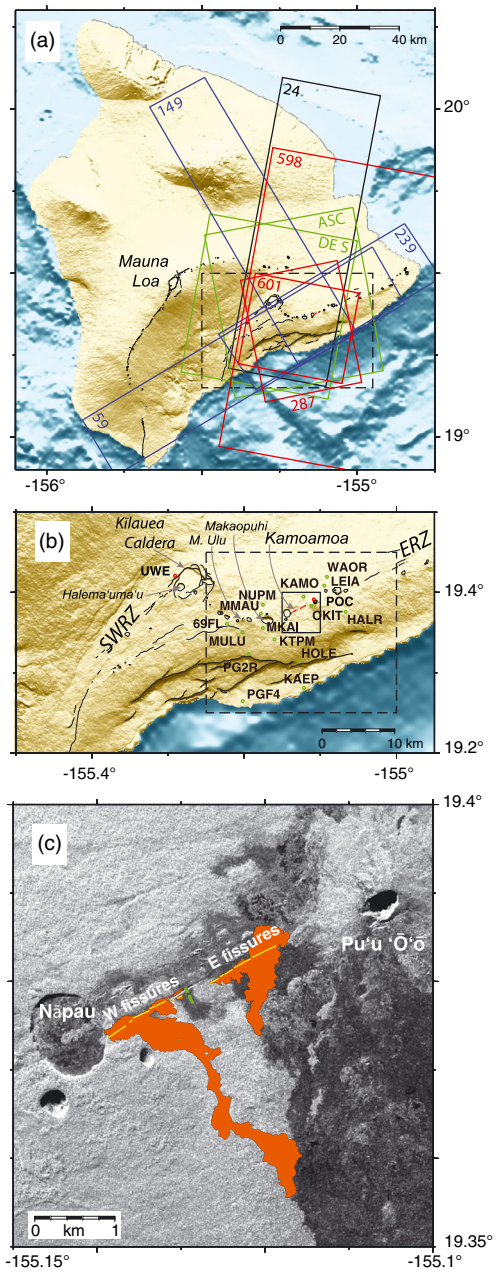

Figure 1. Maps of Hawaii, Kīlauea Volcano, and the Kamoamoa eruption area. (a) Satellite and airborne SAR processed scenes: in red, ALOS tracks; green, COSMO-SkyMed; black, TerraSAR-X; and blue UAVSAR. Track numbers or labels are adjacent to scenes in corresponding colors. Dashed box outlines area shown in Figure 1b. (b) Close-up view of Kilauea, showing GPS sites (green dots); tilt meter sites (red dots); and the Kamoamoa fissures (red lines). Dashed box shows the interferogram area displayed in Figures 4 and 5, and the smaller solid box is the area shown in Figure 1c. SWRZ and ERZ indicate the southwest rift zone and east rift zone, respectively. (c) Close-up view of the fissures and lava flows of the Kamoamoa eruption, overlaying a UAVSAR amplitude image. Mapped fissures, yellow lines; lava flows, orange; and green dots (that appear as two lines perpendicular to the fissures) are the profile locations of the crack opening measurements shown in Figure 16.

propagation require temporal sampling that approaches continuous to resolve deformation progression in the initial hours of an intrusion [*Segall et al.*, 2001]. Recent models have relied on in situ Global Positioning System (GPS) and tilt data to constrain the temporal evolution of dike opening [*Montgomery-Brown et al.*, 2011].

[4] Following several months of summit inflation (Figure 2), a new fissure eruption in March 2011 interrupted Kīlauea's ongoing (since 1983) east rift zone (ERZ) eruptive activity. At 13:45 on 5 March HST (Hawaii Standard Time; UTC 10:00), a tiltmeter on the north flank of Pu`u `Ō`ō began recording rapid deflation, and the floor of Pu`u `Ō`ō crater started to collapse. About 25 min later, Kīlauea summit began to deflate (Figure 3). Magma from both locations appears to have fed an intrusion that reached the surface shortly after 17:00 HST, resulting in an eruption along a set of eruptive fissures ~2 km in length located between Nāpau crater and Pu`u `Ō`ō cone (Figure 1). The activity, designated the Kamoamoa eruption, jumped between fissure segments and effused about 2.7×10^6 m^3 of lava (dense rock equivalent; based on lava flow area and average flow thickness) until all activity terminated on the night of 9 March and the summit began to inflate (Figure 3).

[5] A significant number of geodetic datasets span the Kamoamoa eruption that can constrain dike source models. In addition to GPS and electronic borehole tiltmeter data, an InSAR data set that is comprehensive in temporal sampling and viewing geometry exists for this eruption from the Italian Space Agency (ASI) COSMO-SkyMed (CSK),

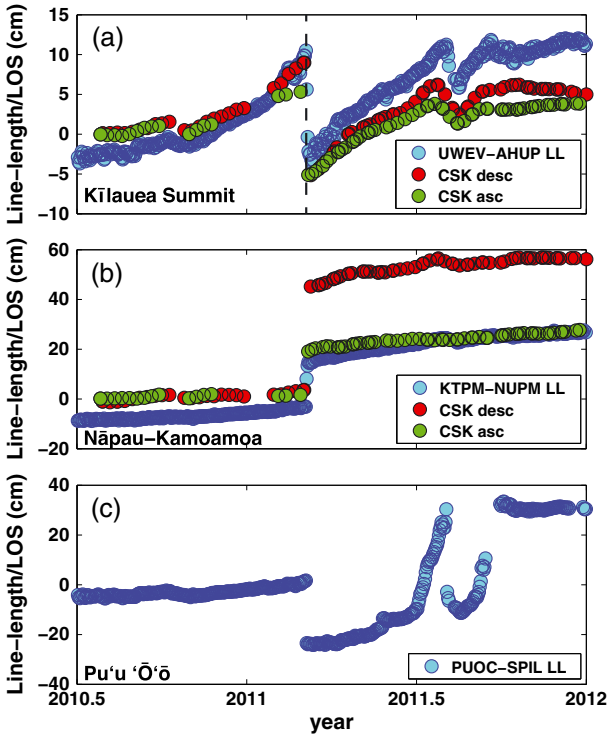

Figure 2. The GPS line-length (LL) and InSAR time series for COSMO-SkyMed ascending and descending data for (a) Kīlauea summit, (b) east rift zone near Nāpau Crater and the Kamoamoa eruption, and (c) across Pu`u `Ō`ō Crater. InSAR time series analysis is described in the auxiliary material.

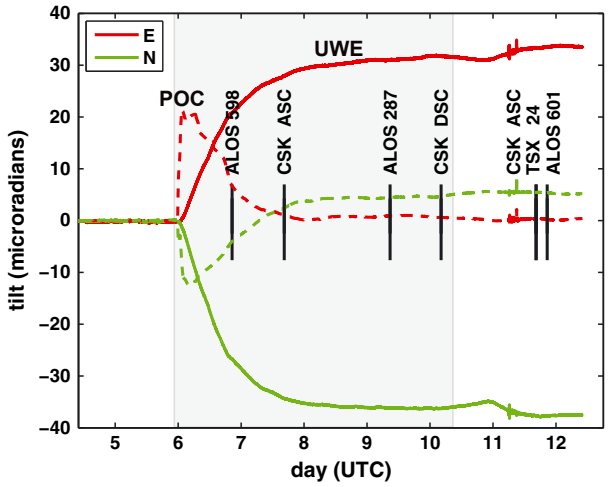

Figure 3. Electronic borehole tilt records for two stations: UWE, located at Kīlauea summit, near the NW edge of the caldera, which shows exponentially diminishing tilt toward the deflating caldera; and POC located near Pu`u `Ō`ō crater and near the Kamoamoa eruption, which shows initial deflation of Pu`u `Ō`ō followed by a change in tilt due to the dike intrusion. Red and green traces show the east and north tilt components, respectively. Black bars indicate the timing of satellite SAR data acquisitions. Gray marks the approximate time interval over which the dike injection and eruption occurred (approximately 5 March 21:30 to 10 March 06:00).

German Aerospace Center (DLR) TerraSAR-X (TSX), Japan Aerospace Exploration Agency (JAXA) Advanced Land Observation Satellite (ALOS) Phased Array L-band Synthetic Aperture Radar (PALSAR), and U.S. National Aeronautics and Space Administration (NASA) Uninhabited Aerial Vehicle Synthetic Aperture Radar (UAVSAR) sensors. Satellite data acquired during or shortly after the eruption include (UTC dates) ALOS on 6, 9, and 11 March, CSK on 7, 10, and 11 March, and TSX on 11 March, all from a mix of ascending and descending tracks (Figure 3; Table S1 of the auxiliary material).[1] UAVSAR airborne data were acquired over a week-long period in early May 2011.

[6] We use InSAR and GPS observations to resolve dike opening at discrete times during, and in the 2 months following, the 5–9 March 2011 Kamoamoa fissure eruption. Modeling was conducted in two steps: first, resolving a single tensile dislocation to constrain the dike dip angle, and second, developing a model that allows for distributed opening of the Kīlauea rifts and décollement, focusing on the area of the Kamoamoa eruption. These models allow us to resolve both the distribution of dike opening within 3 km of the surface and the progression of dike volume over distinct time intervals.

2. Data

2.1. InSAR

[7] InSAR has been widely used to measure relative surface displacements between data acquisitions projected into the radar line-of-sight (LOS), with 1–100 m surface pixel sampling, 20-100 km swath widths, and approximately sub-centimeter precision (depending on radar wavelength) [*Rosen et al.*, 2000]. Along-track (azimuth direction) pixel offsets can also be computed for large (meter-level) deformation to yield horizontal displacements that are perpendicular to the LOS projection plane [*Fialko et al.*, 2001; *Sandwell et al.*, 2008].

[8] We use SAR data from satellite and airborne systems. ALOS PALSAR, CSK, and TSX images were used to compute interferograms and azimuth offsets from pairs spanning approximately 1–2 months that end during or immediately after the Kamoamoa eruption (Figure 3). Airborne data from the NASA UAVSAR sensor were collected in January 2010 and early May 2011.

[9] Satellite SAR data were processed into differential interferograms using the Jet Propulsion Laboratory (JPL)/California Institute of Technology (Caltech)-developed ROI_PAC software version 3.1. Image pairs generally had orbital baseline separations that were less than 200 m. Topographic and orbit geometry phase delays were removed from the interferograms using a 5 m resolution DEM (http://csc.noaa.gov/dataviewer/webfiles/metadata/HI_Ifsar_dtm.html) and using the precise orbits that come with each data product. For the high-resolution COSMO-SkyMed and TerraSAR-X data (both X-band sensors, wavelength 3.1 cm; pixel size ~2 m) we take four "looks" (number of pixels being averaged) each in range and azimuth directions (cross- and along-track, respectively) to improve signal-to-noise ratio and to facilitate phase unwrapping. ALOS (L-band, wavelength 23.6 cm, pixel size ~6 m) interferograms were processed at one look in range and two looks in azimuth (no averaging of squared pixels). We unwrapped each interferogram using either the SNAPHU software [*Chen and Zebker*, 2001] or the default ROI_PAC branch-cut unwrapper [*Goldstein et al.*, 1988] for the TSX data (due to constraints on the total number of pixels that could be unwrapped with SNAPHU). Each satellite interferogram was weakly filtered using a power spectrum filter [*Goldstein and Werner*, 1998] with a filter exponent value of 0.5. This improved the performance of both unwrappers, especially for the default branch-cut unwrapper in the case of the TSX interferogram.

[10] The UAVSAR instrument is attached to a Gulfstream III aircraft that uses a precision autopilot designed for repeat pass interferometry applications [*Hensley et al.*, 2007]. UAVSAR differential interferograms are computed by the NASA UAVSAR Project at JPL. Interferogram swath widths are approximately 20 km and their length is typically on the order of 100 km. Interferograms are computed to a geocoded pixel sampling of ~5.6 m. Due to the long temporal separation of the UAVSAR acquisitions (early January 2010 to early May 2011), significant phase noise is evident in the unfiltered interferograms in highly vegetated areas on Kīlauea. The UAVSAR wavelength (23.8 cm) allowed unwrapping of the broad fringes after applying a power spectrum filter (filter strength 0.7) twice before unwrapping with the ROI_PAC branch-cut methodology. The stronger filtering was required to improve spatial completeness without introducing spurious phase artifacts.

[11] The unwrapped interferograms used in this study are shown in Figures 4 and 5, with a color cycle (fringe rate) of 10 cm. Due to the large number of pixels in each interferogram and azimuth offsets (on the order of one million), we

[1]Auxiliary materials are available in the HTML. doi:10.1029/2012JB009616.

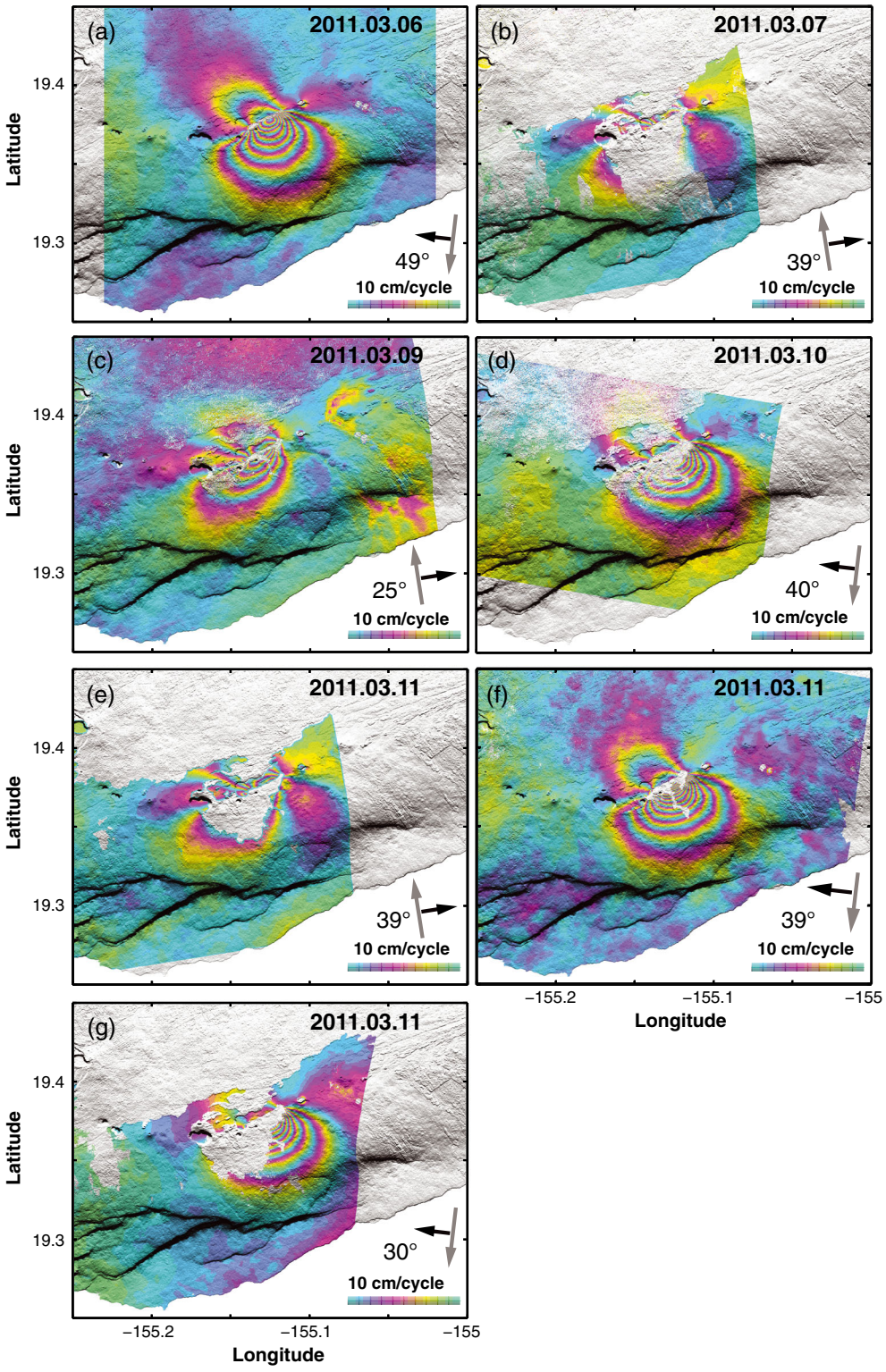

Figure 4. Satellite SAR interferograms over shaded relief for the dashed box area shown in Figure 1b. Interferograms are depicted with a 10 cm color cycle. In each panel, gray/black arrows indicate the satellite heading and look directions, respectively, and the approximate incidence angle, from vertical, in the center of the image. Ending date shown in the upper right corner. Original ALOS PALSAR data is copyright (2010, 2011) JAXA, Minestry of Economy, Trade and Industry (METI). Original TerraSAR-X data is copyright (2011) DLR. Original COSMO-SkyMed data copyright (2010, 2011) ASI. (a) ALOS, track 598, 2011.01.19-2011.03.06 (yyyy.mm.dd); (b) CSK, ascending track, 2011.02.11-2011.03.07; (c) ALOS, track 287, 2010.12.07-2011.03.09; (d) CSK, descending track, 2011.02.14-2011.03.10; (e) CSK, ascending track, 2011.02.03-2011.03.11; (f) ALOS, track 601, 2011.01.24-2011.03.11; and (g) TSX, track 24, 2011.01.04-2011.03.11.

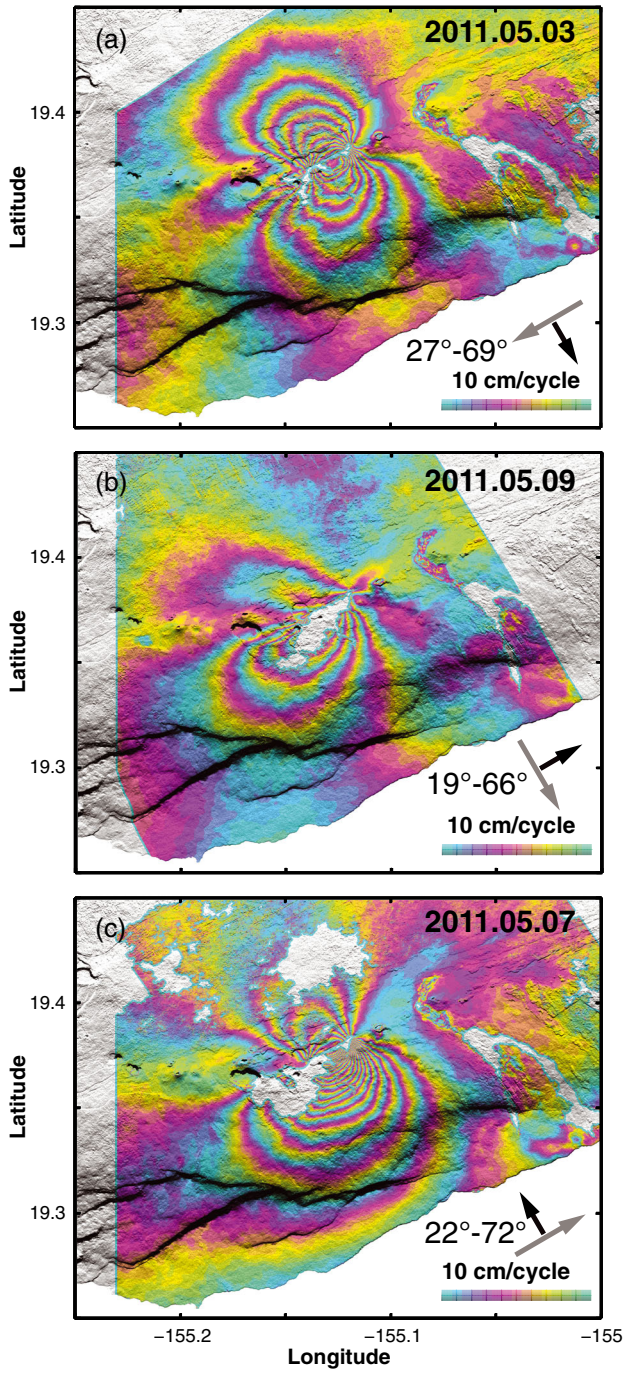

Figure 5. Airborne UAVSAR interferograms over shaded relief, for the dashed box area shown in Figure 1b. Interferograms are depicted with a 10 cm color cycle. In each panel, the gray/black arrows indicate the aircraft heading and look directions, respectively, with the approximate range of incidence angles, from vertical. Ending date shown in the upper right corner. (a) 2010.01.06-2011.05.03; (b) 2010.01.06-2011.05.09; and (c) 2010.01.04-2011.05.07.

use a model-based quad-tree approach [*Lohman and Simons*, 2005] optimized to resolve deformation for the dike to down-sample each interferogram to 1000–2000 data points and compute data covariances. For the Kīlauea deflation down sampling, the model was a 2×1.8 km (width and length) sill at 2 km depth, and for the Kamoamoa dike down sampling, the model was a vertical dike following the eruption fissures with an along-strike length of 6.5 km and a width of 20 km to give smooth fall-off in the spatial sampling density. One-standard deviations for the quad-tree down-sampled data are not plotted, but were generally in the 1–3 mm, 2–8 mm, and 80–120 mm range for CSK/TSX, ALOS, and azimuth offsets, respectively. These formal uncertainties we consider to be too small since they do not account for the phase noise in the pre-filtered data or atmospheric phase delays.

2.2. GPS

[12] Daily positions of GPS sites were used to compute displacements between dates corresponding to interferogram dates, except for interferograms formed with scenes from 6 March 2011 UTC—the day the intrusion started. Because of the high displacement gradients on 6 March, we computed sub-daily positions and used the positions closest to the acquisition time of the SAR scene to calculate displacements.

[13] Both daily and sub-daily GPS solutions were computed using the GIPSY/OASIS II software package developed at the Jet Propulsion Laboratory in point-positioning mode [*Gregorius*, 1996; *Zumberge et al.*, 1997]. Pacific Plate motion was removed by subtracting the average motion of IGS site MKEA on Mauna Kea. For the daily processing, we used non-fiducial orbits and transformed the solutions into a global ITRF2008 reference frame with a seven-parameter Helmert transformation using daily parameters provided by JPL. For the sub-daily processing, we used ITRF2008 orbits and estimated position as a stochastic parameter, applying smoothing through a random walk parameterization, with position updates every 10 min.

[14] The formal errors of the GPS daily solutions are generally considered too small compared to the scatter in the GPS time series. Rather than simply scale the GPS formal errors by an arbitrary factor, we chose to estimate the uncertainty for each component based on its one-standard deviation over ± 14 days for the daily solutions and 3 h for the sub-daily solutions (dashed lines in Figure 6). Typical one-standard deviations were approximately 2 mm in the east (E) and north (N) directions, and 7 mm in the up (U) direction.

3. Modeling

[15] To model the Kamoamoa dike we followed a two step process: (1) solve for a simple planar tensile dislocation and (2) develop a whole-Kīlauea rift and décollement distributed opening model, with the eastern ERZ (from the Kamoamoa fissure area eastward) conforming to the co-eruptive dip determined in the first step.

3.1. Simple Model

[16] To solve for the simple tensile dislocation with uniform opening, we used a Markov chain Monte Carlo (MCMC) approach to search the model parameter space using the method of *Fukuda and Johnson* [2010]. Histograms of retained solutions produce probability density functions for each parameter. We use the mapped surface locations of the eruptive fissures as a priori constraints on the location of the dike, with the strike held fixed. If we assume the dike to be planar, then we need to solve for the dip of the dike to have

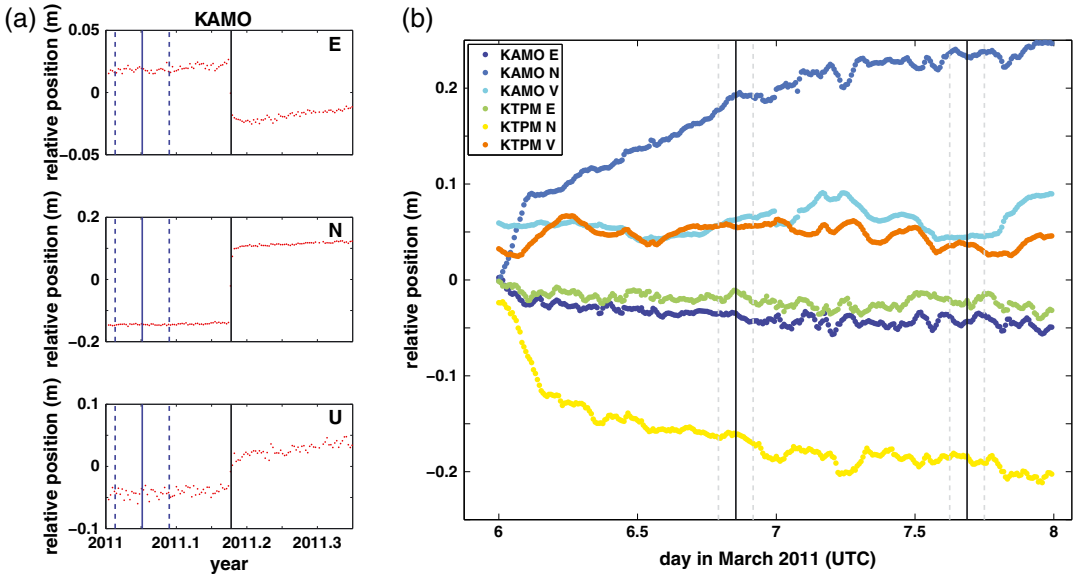

Figure 6. (a) The GPS daily solution time series spanning the March 2011 eruption for station KAMO, one of the sites with the largest displacements. For displacement calculations differences are calculated between the times indicated by the black and blue solid lines (in this example for the 6 March 2011 ALOS interferogram time interval) and the GPS component standard deviation and mean value are calculated for the portion of the time series ±14 days depicted by the dashed blue lines (for 6 March, only the single day is used; see text for details). (b) GPS sub-daily, 10 min time series (6–7 March) for the two stations with the largest displacements (KAMO, KTPM). Solid black lines are the times of the SAR acquisitions on 6 and 7 March. Dashed gray lines define the 3 h interval centered on each SAR time for which the mean relative position and standard deviation are calculated (with displacements calculated relative to the InSAR starting date sub-daily GPS solutions that are not shown). The entire time window shown in Figure 6b is equivalent to the time spanned by the two daily solutions following the vertical solid line marking the eruption start in Figure 6a.

a good starting geometry for more complex models of distributed opening. For the MCMC parameter estimation we used the down-sampled ALOS ascending (7 December 2010 to 9 March 2011) and descending (24 January 2011 to 11 March 2011) interferograms spanning the eruption. The GPS displacements are calculated for the time interval of the descending ALOS interferogram. All modeling is done in a local Cartesian coordinate system with distance measured relative to HVO (longitude −155.288, latitude 19.42) on the NW rim of Kīlauea Caldera. The best fit solution from one million kept models (Figures S1–S3) dips 72° to the SE, with no weighting given to the GPS data relative to the InSAR data. For purposes of constraining the dike dip, the denser InSAR data are better suited near the shallow portion of the dike than the more dispersed GPS sites. In this sense, the GPS data serve more to show the fit (or lack thereof) of the InSAR-dominated simple dislocation solution to the GPS. The fit is not very good and reflects the inability of a single dislocation with uniform opening to adequately fit the data. The dip that we find is somewhat shallower than previous ERZ dikes, for example, 80° for ERZ dikes emplaced in 2007 [*Montgomery-Brown et al.*, 2010] and 1999 [*Cervelli et al.*, 2002], and 76° for a dike associated with a fissure eruption in 1997 [*Owen et al.*, 2000a].

[17] It should be noted, as shown in Figure S2, that all parameters except the strike are effectively estimated—with the depth fixed at the surface and the width and dip angle determining the depth to the lower edge. Given the coarseness of the data and potential trade-offs with the assumptions of a simple rectangular dislocation, perfect alignment with the observed surface fissures may not occur without fixing the *easting* and *northing* locations as well.

3.2. Distributed Dike Opening/Fault Slip Modeling

[18] After determining the basic geometry of the dike, the next step is to solve for a distributed dike model by using a larger fault than determined in the MCMC result. The surface position and strike of the dike are based on the location and strike of the eruption fissures, and the dip is based on the solution in the previous section. We discretize this larger fault into smaller elements and apply a Laplacian smoothing operator to regularize the non-negative least squares inversion. We choose a smoothing parameter that balances the spatial roughness of tensile opening with the reduction in data misfit [*Jónsson et al.*, 2002]. We initially tried a number of models using a simple planar dike broken into a regular grid of rectangular patches. For the co-diking models, this solution would fit the InSAR data quite well but had difficulty fitting some of the larger GPS displacements (for example, at sites KTPM and HOLE, located ~2–5 km SSW of the eruption location). When we expanded our modeling to include the UAVSAR data and its longer time span (and hence greater secular flank motion), it became necessary to apply a more realistic model that better captured the main structures of

Kīlauea, including the southwest and east rift zones as well as the horizontal basal detachment fault at ~9 km depth [*Syracuse et al.*, 2010]. This model extends well beyond the data used to model the Kamoamoa dike and requires that we apply much higher slip smoothing in areas beyond the resolution of our data to prevent spurious slip (Figure 7). The smoothing parameters for the model areas outside the Kamoamoa eruption segment were determined through trial and error. To determine the least amount of smoothing over the ERZ segment spanning the Kamoamoa eruption, we varied the smoothing factor that weights smoothness versus data misfit through a range of reasonable solutions, finding the point that is near the point of maximum curvature: the "corner" in the L-curve of data RMS misfit versus fault displacement roughness (Figure 8) [*Jónsson et al.*, 2002]. We mesh the curved fault surfaces of the rift using the open source Matlab program Mesh2d that allows for an irregular triangular mesh of multiple planar sections, which we then modified to warp smoothly for along-strike variations in dip angles. The use of a single structure to model the rift zones oversimplifies the structural complexity of the SE flank [*Morgan*, 2006] both in the number and geometry of active structures and their relation to the complexity and geometry of the dike intrusions [*Montgomery-Brown et al.*, 2009]. The rift zones of Kīlauea are usually modeled as being vertical, but numerical simulations of flank motion suggest SE dipping structures are to be expected, both within and at the back of the flank wedge [*Morgan*, 2006].

[19] We compute models for each of the dates during the eruption (6, 7, and 9 March) and a single model for the four interferograms immediately after the end of the eruption (10 and 11 March). We also compute a model for the UAVSAR interferograms stemming from data collected over

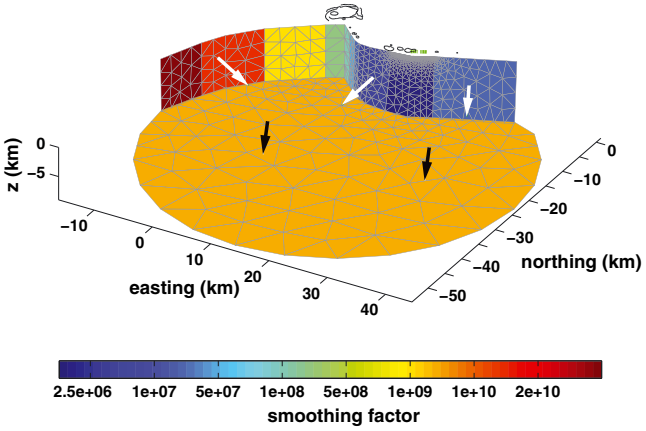

Figure 7. Model setup for the whole-volcano model. In this perspective view from the SE, the SW and E rift zones appear as curved near vertical structures, while the horizontal detachment is a partially circular disk 9 km beneath the surface. Color indicates the smoothing factor—blue means less smoothing, red more, and arrows show the type of displacements allowed in the model: white indicating tensile opening of the rifts and black showing the direction of horizontal shear of the detachment. Easting and northing are measured relative to HVO (longitude −155.288, latitude 19.42) on the NW rim of Kīlauea crater.

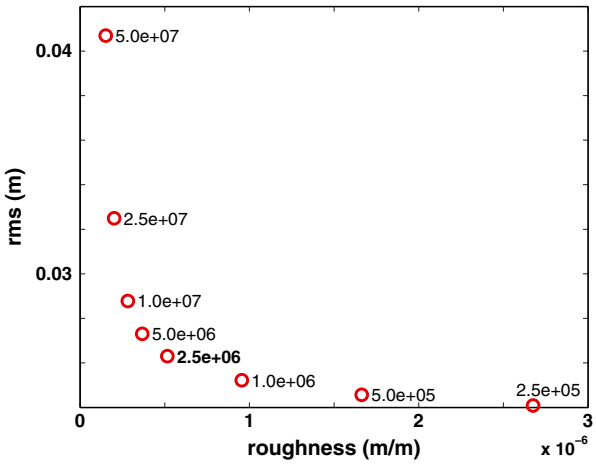

Figure 8. Solution root-mean-square misfit versus fault slip roughness as a function of the smoothing value for the Kamoamoa section of the ERZ (darkest blue in Figure 7). The value indicated in bold type (2.5×10^6) is the value used in all models.

1 week periods in early January 2010 and early May 2011. Each of these models also uses the three-component GPS displacements that match the time spans of the interferograms. For the four interferograms on 10–11 March, we use a starting date of 24 January (in the middle of the interferogram start dates) and an ending date of 11 March. The UAVSAR-constrained model uses GPS displacements from 6 January 2010 to 3 May 2011. In each model, the fault slip smoothing is the same as in Figure 7 and the GPS data are weighted by a factor of 10 relative to the InSAR data. For dates with a single set of SAR data, we used both the unwrapped phase LOS displacements and the azimuth offsets (the latter being much noisier), along with the GPS displacements.

[20] We applied the whole-volcano model (Figure 7) based on evidence for large-scale flank motion defined mechanically by the rift zones and the basal detachment [e.g., *Owen et al.*, 200b]. This model was considered important for the long time interval covered by the UAVSAR data. One effect of this model and the variable smoothing that we impose is the possibility that the assumptions of smoothing and geometry may skew model resolution. Because we use a nonlinear inversion for the model displacements, we are not able to solve for model resolution directly as for linear least squares inversion [*Page et al.*, 2009]. Instead we generate synthetic data from a variable size "checkerboard" distribution of unit displacements and invert these synthetic data to see how well our inverse model compares to the known input model (Figure S4). Much of what we find is expected: large smearing of fault displacements in areas of large smoothing (i.e., the SW rift zone and the detachment plane). We also find reduced resolution at depth as expected. A more surprising effect is the reduced resolution of the deeper half of the ERZ beneath the area of the Kamoamoa dike intrusion. This appears to be due to a trade-off between detachment slip and deep rift opening. In the model without the detachment (Figures S4b, S4d, and S4f) some of the deep ERZ opening is resolved (albeit crudely). In each instance the fit of the inverse surface displacements (not shown for brevity) to the observed is excellent.

4. Results

4.1. Co-Diking Models

[21] The model for the ALOS PALSAR interferogram that ends on 6 March 2011, is shown in Figures 9–11. Figure 9 gives the observed, modeled, and the residual InSAR phase (Figure 9a), InSAR azimuth (Figure 9b), and GPS (Figure 9c) displacements. For the GPS data, uncertainties for horizontal and vertical displacements are shown on the residual plot only. Note that the GPS residuals (Figure 9c, and for all other models presented) are shown at twice the scale as the observed and synthetic to improve visibility of the differences. Figure 10 displays the entire model domain in perspective view, demonstrating that tensile opening in the rifts and SE-directed décollement slip are effectively suppressed outside of the main dike area. In Figure 10a, we show the results for the rift-zone-only model for comparison to the whole-volcano model, which shows that there is very little difference between the two. For all subsequent models we show the rift-zone-only model.

[22] Viewed from the top (Figure 11a), the dip of the dike to the south is apparent, while a cross-section view from the south (Figure 11b) demonstrates the dike deepening in the up-rift (WSW) direction. Seismicity from the HVO catalog (blue dots in Figure 11) is somewhat scattered, but with a significant clustering at about 3 km depth below the deeper SW extension of the dike (Figure 11b). Note that our modeling is done with a half-space approximation, so the depths of the model and un-relocated seismicity are shown relative to zero elevation but are actually relative to the surface which is approximately 800 and 1200 m above sea level for the fissure eruption and Kīlauea summit, respectively. The cross-section view also shows an apparent extension of opening toward Pu`u `Ō`ō (to the east). Dike opening in this area becomes

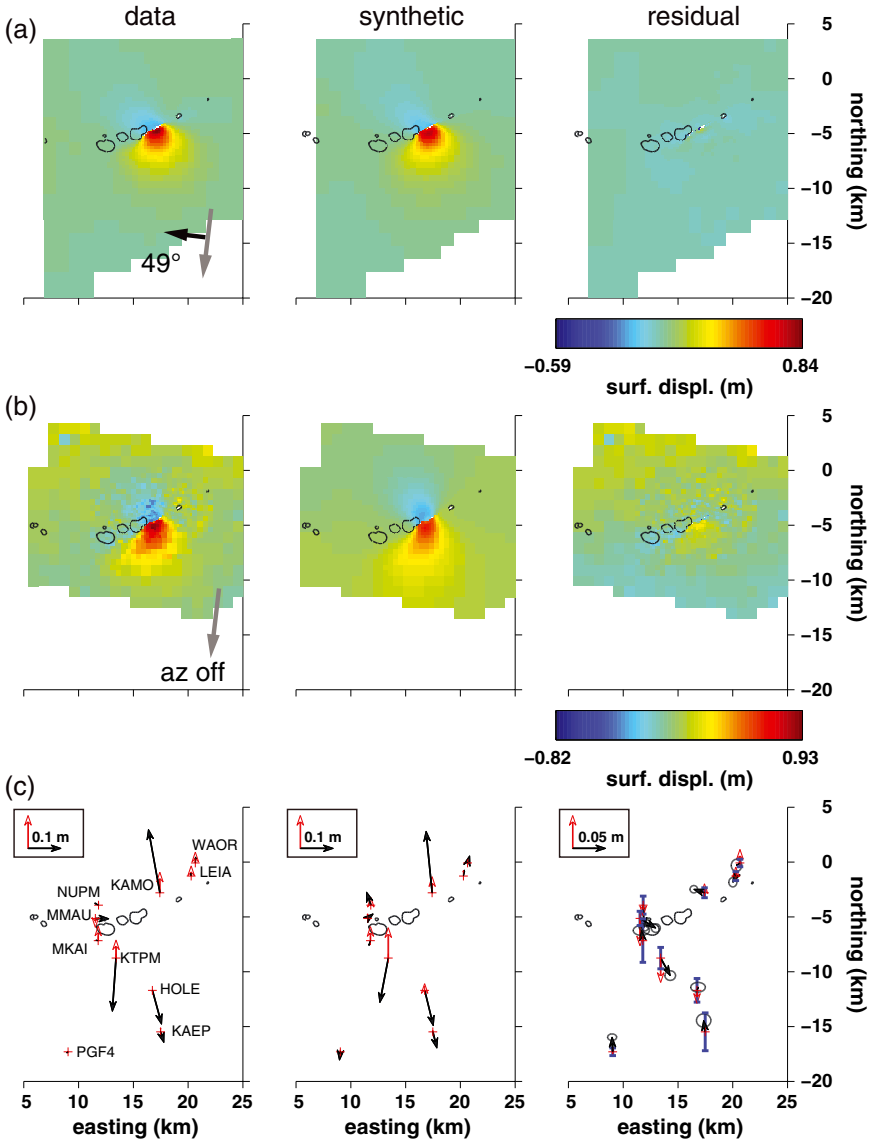

Figure 9. The 6 March inversion results. Data (left column), synthetic (center), and residual (right) for (a) the quad-tree down-sampled ALOS LOS and (b) the azimuth pixel offsets, and (c) the GPS displacements. GPS displacement 2σ vertical and horizontal uncertainties are shown in the GPS residual plot. Note the smaller scale for the GPS residuals.

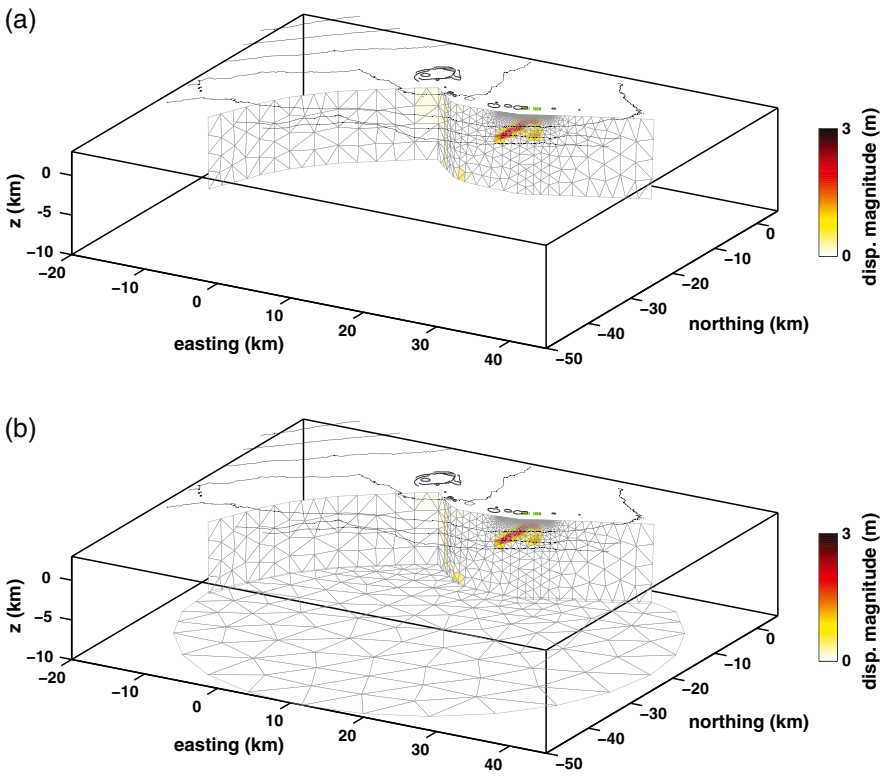

Figure 10. The 6 March modeled dislocation displacement magnitudes for the entire model domain. Topography 500 m contours and outlines of craters shown in black and green indicates the Kamoamoa fissures. (a) Rift-zone-only model solution. (b) Model with the detachment fault included.

more prominent in models spanning later time periods. Key features of this model include (1) deep, strong opening at 2–3 km beneath the surface at the up-rift (west) end of the dike; (2) incomplete opening of the dike at the surface—there are two areas of roughly 1.5 m opening at each end of the mapped fissure zone with an area of reduced opening between; and (3) mid-level (2 km) extension of opening toward the east.

[23] The 7 March 2011 model (Figures S5 and S6) lacks some of the detail of other models due to differences in data weighting and smoothing, but more fundamentally reflects the less complete spatial coverage of the X-band CSK data compared to the L-band ALOS (or UAVSAR) data. In addition, the 7 March data are from an ascending track, which looks along the strike of the dike and is less sensitive to horizontal displacements associated with dike opening. The model does, however, suggest an increase in shallow dike opening compared to the 6 March model and retains the up-rift descent of the dike beneath the surface.

[24] The 9 March 2011 model is similar to that of 7 March in that it is also from ascending track data, however the improved coherence of this ALOS scene results in improved spatial coverage (Figure S7). Modeled opening of the dike is, therefore, more continuous from the up-rift tail at 3 km depth to the surface and is greater than that of the 6 March model and with near-complete opening at the surface (Figure S8).

[25] The 10–11 March model spans the entire eruption and includes four interferograms (azimuth offsets were not included, as they offered little improvement in the modeled dike) as well as the GPS displacements (Figure 12). The dike model (Figure 13) shows an increase in the opening of the dike since 6 March, especially in the shallower portions beneath the Kamoamoa fissures down to about 2 km beneath the surface. There is also increased opening in the area toward Pu`u `Ō`ō (2 km below the surface). The magnitude of dike opening at the surface approaches 3 m.

4.2. May 2011 Models

[26] The final model we examine combines the three UAVSAR interferograms with GPS displacements over 1.4 years. As expected, the GPS data include secular motion of Kīlauea's south flank toward the sea. The UAVSAR data must also include this signal, which would be on the order of 10 cm/yr to the SSE [*Owen et al.*, 2000b] and would result in a fraction of a fringe at L-band over a long spatial scale. There is no obvious displacement due to flank motion, perhaps because UAVSAR processing applies a motion compensation correction during interferogram generation that may remove such a signal, or the flank motion signal in the InSAR data may be masked by either atmospheric effects or by uncompensated aircraft motion. Also, the portion of each interferogram chosen for analysis (Figure 5) is restricted to the area of strongest co-diking deformation, so areas to the SW that might contain pure flank motion are not included. Figure 14 shows the model fit to the data. Despite the long time interval between acquisitions, the UAVSAR interferogram and GPS data are reasonably well fit. We found that increasing the GPS weighting reduces the GPS misfit with minimal increase in InSAR residuals and causes some increased deep opening in the dike model, but for comparison purposes we chose the same smoothing and GPS weighting for all models.

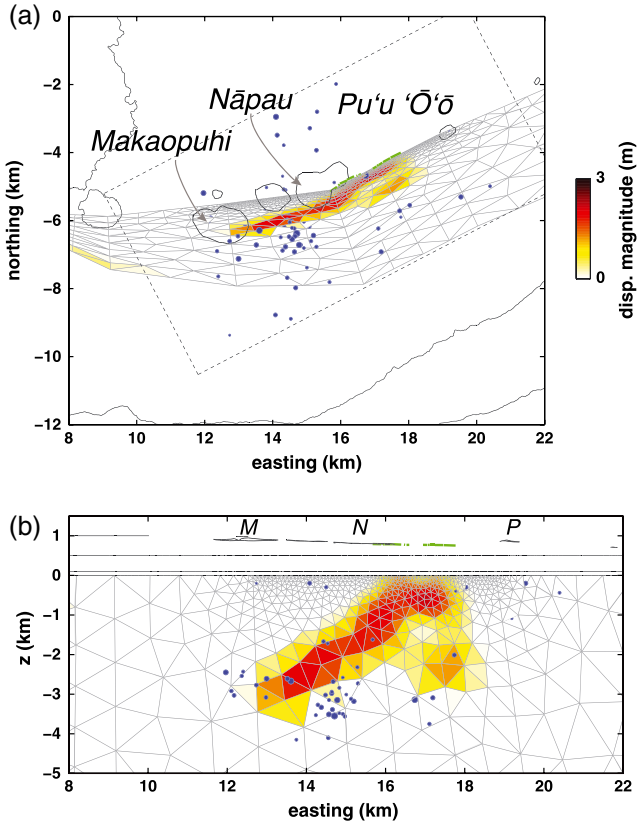

Figure 11. Close-up view of the 6 March rift-zone-only model. (a) Top view showing the steeply dipping dike, and the seismicity (blue circles, size proportional to magnitude) from 5 to 6 March for the dashed box area surrounding the dike intrusion. (b) Side view from the south. Crater outlines and topography contours, and green mapped Kamoamoa fissures show at their true elevations, whereas the dike model is shown within its half-space. *M*, *N*, and *P* indicate the Makaopuhi, Nāpau, and Pu`u `Ō`ō crater locations, respectively.

[27] The one area in the UAVSAR data where the model misfit appears to be significant is shown immediately to the south of the fissure eruption, where the model under predicts the strong negative LOS displacements (Figure 14b). Given that there are no apparent unwrapping errors (made easier to determine at L-band due to the relatively moderate spatial fringe rate) and the horizontal azimuth offsets for the 6 March model were also underpredicted (Figure 9b), the discrepancy probably reflects limitations in the model geometry, assumption of only opening motion, or possibly differences in vertical versus horizontal displacements due to inelastic deformation or difference between the Poisson's ratio of the rocks and the 0.25 value used in the elastic model. The full-resolution interferograms (not resolvable in Figures 4 and 5) show a large number of dike-parallel fractures within a couple of kilometers of the dike to the SE. There is also evidence for a splay fault curving south and southwestward for 2–3 km from the western end of the active fissures. These structures may have played a role in accommodating the surface displacements that are not accounted for in our single structure model.

[28] The model also indicates increased deep rift opening away from the Kamoamoa eruption site, suggesting an attempt by the model to fit the broader flank motion present in the GPS data (Figure 15a). The dike itself (Figure 15b), however, is similar to the 6 March (Figure 11b) and 10–11 March (Figure 13b) models, with approximately 3 m opening at the surface but with increased opening to nearly 3 km below the fissure eruption site. Additional opening to 4 km depth in the deeper up-rift (WSW) direction is not well constrained by these data, as supported by the checkerboard test (Figure S4).

4.3. Dike Surface Opening Progression

[29] A robust feature of the dike models lies in the shallowest 1 km beneath the eruptive fissures, where an increase in dike opening from the 6 March to 10–11 March models is apparent (Figure 16). Field measurements of total crack/fissure opening along a profile perpendicular to the strike of the dike and located between the two primary fissure segments (Figure 1), where no lava erupted but the dike was likely just beneath the surface, on 6 March and 9 March (HST or approximately 00:00 7 March and 00:00 10 March UTC) found approximately 1.4 m and 2.7 m, respectively (Figure 16)—very close to the modeled opening at the surface for 6 March and 10–11 March. The UAVSAR model indicates a similar dike surface opening profile as the 10–11 March model, indicating that no additional opening occurred at the surface between the end of the eruption and May (at least, within the resolution of our modeling, the details of which should be interpreted with caution in light of the heterogeneous data sets and the relative effects of using the same GPS data weights and smoothing factors).

5. Discussion

[30] Dike volume change, propagation, and whether or not the dike remains confined to the subsurface or reaches the surface in a fissure eruption depend on many factors including confining stresses, source volume and pressure, the distance to and openness of the feeding conduit, and fracture toughness [*Rubin and Pollard*, 1987; *Rubin*, 1993; *Segall et al.*, 2001]. Our models constrained by InSAR and GPS data during and following the March 2011 dike intrusion and fissure eruption provide a detailed view of the distribution of dike opening over discrete times. When combined with knowledge of past events and the plumbing of the Kilauea-ERZ system, our results provide constraints on the sources and processes controlling dike intrusions into the ERZ.

5.1. Dike Volume Change

[31] Continuous temporal observations of surface deformation from tilt or GPS are often used to constrain models of dike growth and provide insight into both the physics and geometry of dike emplacement [*Segall et al.*, 2001; *Desmarais and Segall*, 2007; *Montgomery-Brown et al.*, 2011]. The in situ tilt and GPS networks at Kīlauea have been at the forefront in these efforts, with the improved spatial coverage of InSAR previously limited to constraining the total deformation, and with the in situ data providing the temporal coverage [e.g., *Montgomery-Brown et al.*, 2011]. The data set available for the Kamoamoa eruption offers improved InSAR temporal sampling during the fissure eruption, although it still does not cover the initial stages of dike propagation prior to the onset

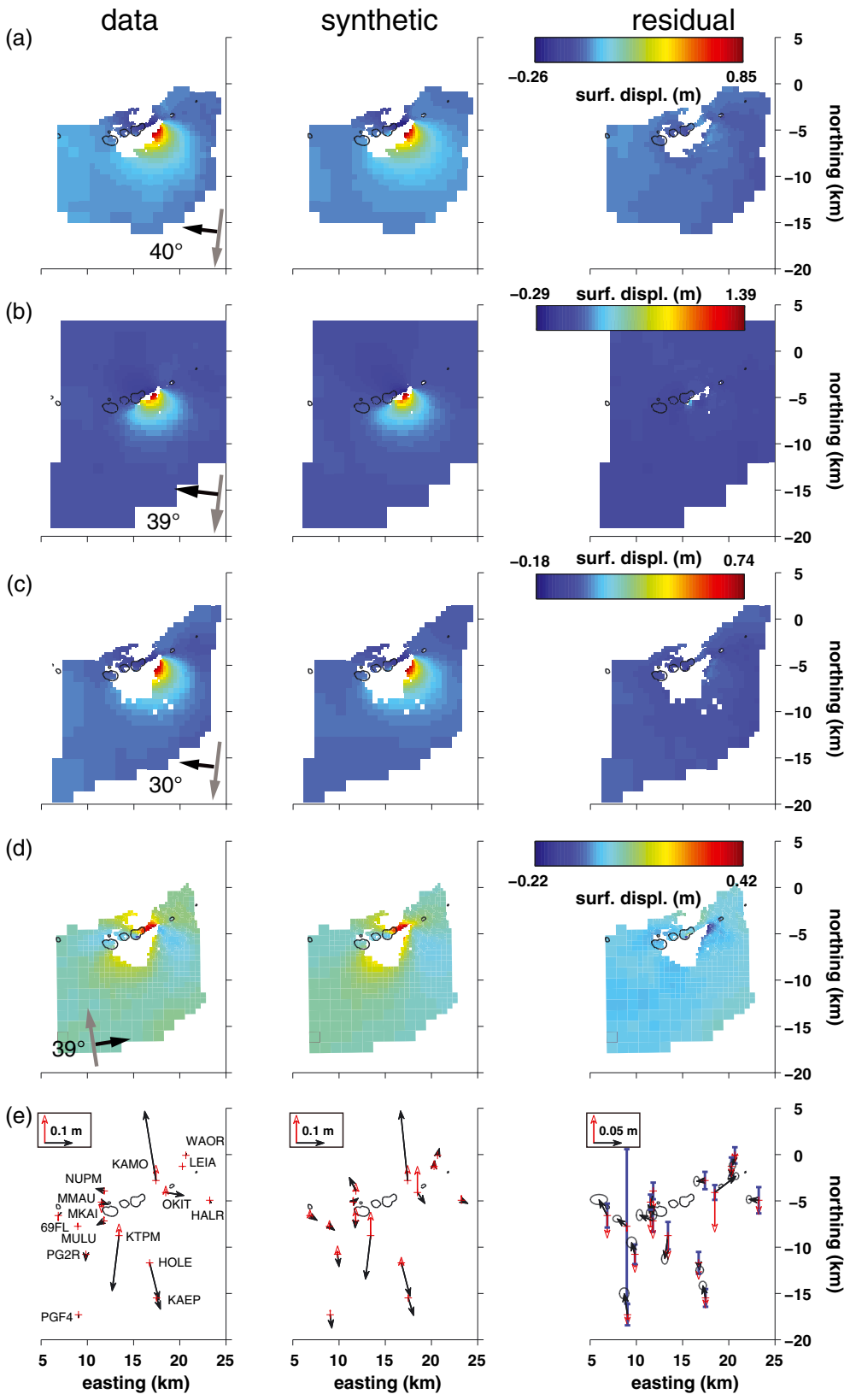

Figure 12. The 10–11 March rift-zone-only model inversion results. Format the same as for Figure 9. (a) CSK descending; (b) ALOS descending; (c) GPS; (d) TSX descending; and (e) CSK ascending.

of eruptive activity—the most critical time interval for understanding the physics of dike propagation [*Segall et al.*, 2001; *Larson et al.*, 2010]. In this study, we model the dike as a set of independent static models allowing us to investigate the evolution of the dike over the several days duration of the eruption and in the post-eruption time period.

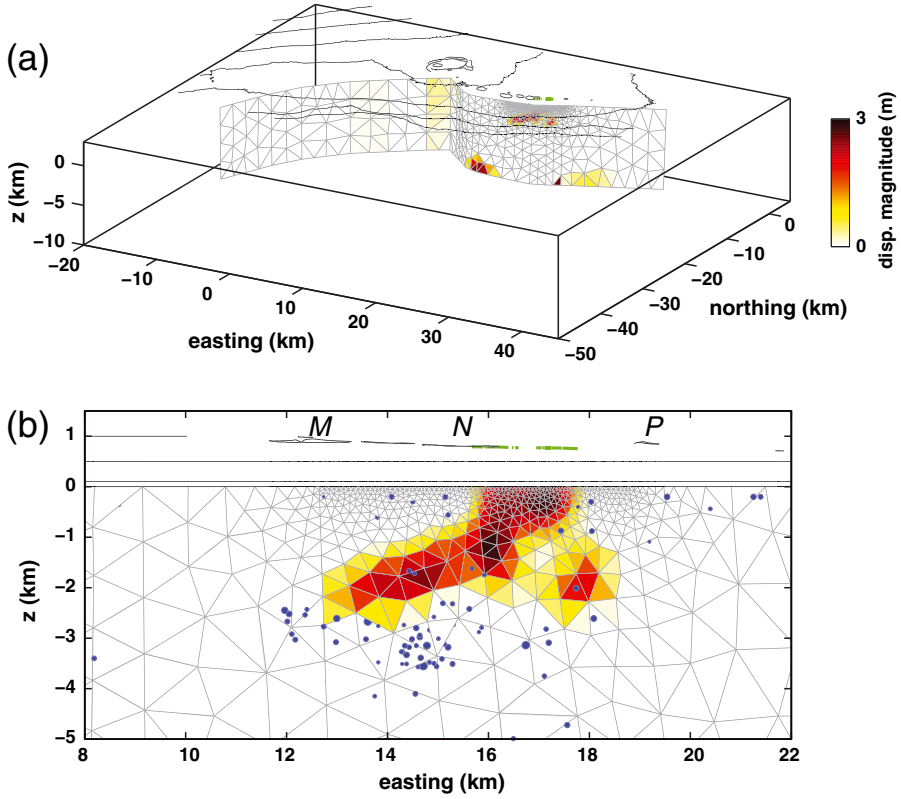

Figure 13. The 10–11 March modeled dislocation magnitudes. (a) Entire model domain, perspective view. (b) Close-up side view from the south. Seismicity (blue circles) is shown for 5–11 March. *M*, *N*, and *P* indicate the Makaopuhi, Nāpau, and Pu`u `Ō`ō crater locations, respectively.

[32] The dike volumes calculated for the five models during and after the eruption show an increase in model volumes with time that suggests a roughly linear to slightly decaying rate of volume increase (Figure 17), except for the 7 March model, which is the least constrained due to less complete InSAR coverage. The volume increase over time is similar to the GPS surface deformation time series (Figure 6), where we see that by the time of the first InSAR data roughly 17.5 h into the eruption (~22.5 h into the intrusion) most of the dike volume had already been intruded. This has some similarities to the volume increase modeled for the 1997 dike intrusion [*Segall et al.*, 2001] where they found that two thirds of the dike volume accumulated prior to the eruption. However, in this case we find that by the time of the 6 March SAR data, the dike volume was 95% and 70% of its volume at the end of the eruption and in early May, respectively. In the case of the 1997 event, dike volume growth had essentially stopped by the end of the 22 h eruption [*Segall et al.*, 2001], whereas we find increased volume over the 2 months following the end of the eruption.

[33] Also similar to the 1997 event, tilt data at the summit and Pu`u `Ō`ō are characterized by rapid exponential decay (Figure 3) in the initial 24 h, with summit tilt becoming nearly flat 2 days into the 4 day eruption. The 2011 Kamoamoa eruption tilt signal is consistent with *Segall et al.'s* [2001] model of a large volume, large compressibility magma reservoir coupled to a propagating dike through an open conduit with high driving pressure, but does not explain the prolonged dike volume increase that we find for the Kamoamoa eruption.

[34] During and immediately after the Kamoamoa eruption, continued opening of the initial dike occurred in the deeper part of the dike between Makaopuhi and Pu`u `Ō`ō craters. This is evident in the 6 March to 10–11 March models (Figures 11b and 13b). As the dike volume increases into May 2011 (Figure 15b), additional areas of dike opening appeared at greater depth in the immediate up-rift direction and below the eruptive fissures. This is also apparent in dike model profile at the surface, 0.5 km, and 2 km depth for the models of 6 March, 10–11 March, and early May (Figure S9). In Figure S9, we see that near the end of the first day of the eruption opening within the dike from 0.5 to 2 km depth is around 2 m, with decreased opening at the surface. Immediately after the eruption (10–11 March) dike opening has reached its maximum of around 2.8 m at all depths. The May profiles are similar to the 10–11 March ones, but with enhanced 2 km opening around 16 km easting, roughly below the western end of the fissure eruption. Part of this opening may reflect artifacts from model assumptions (e.g., elastic half-space, imposed dike/fault structures), inadequate spatial coverage, and noise sources in the data. These assumptions may limit model resolution and possibly lead to spurious sources of dike opening. If we consider only the area within the volume calculation region outlined by the dashed box in Figure 15b where the InSAR data provide strong constraints, we see an increase in opening both at the western terminus of the dike and directly beneath the main fissures (>2 km beneath the surface). These two areas coincide with the area of greatest co-diking seismicity. Without putting too much confidence in the details of the model, the results suggest that the source of magma driving the continued dike opening came from greater depth in both

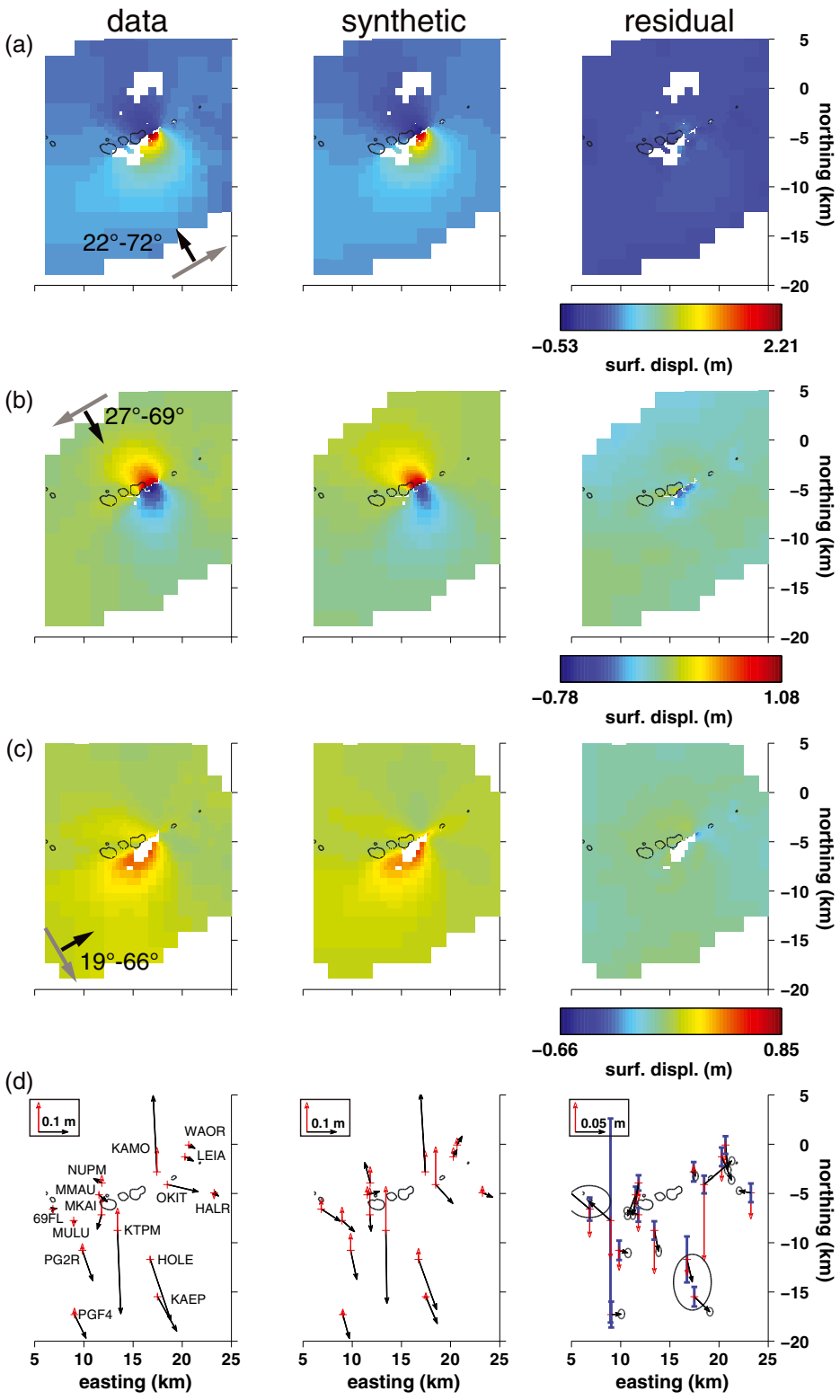

Figure 14. May 2011 UAVSAR and GPS results. Format the same as for Figure 9. (a) Flight line 059; (b) flight line 239; (c) flight line 149; and (d) GPS.

the up-rift direction and from beneath the dike, in addition to a possible contribution from an area at 2 km depth in the down-rift direction toward Pu`u `Ō`ō crater. If there is a continuous magma conduit from Kīlauea's summit to Pu`u `Ō`ō, the May 2011 model would suggest continued intrusion from this conduit into the deeper central portion of the co-eruptive dike intrusion in the 2 months following the eruption.

[35] The dike volumes that we model can also be compared to the volume loss estimates for magma sources that fed the dike: beneath Kīlauea's summit and Pu`u `Ō`ō. Solving for a

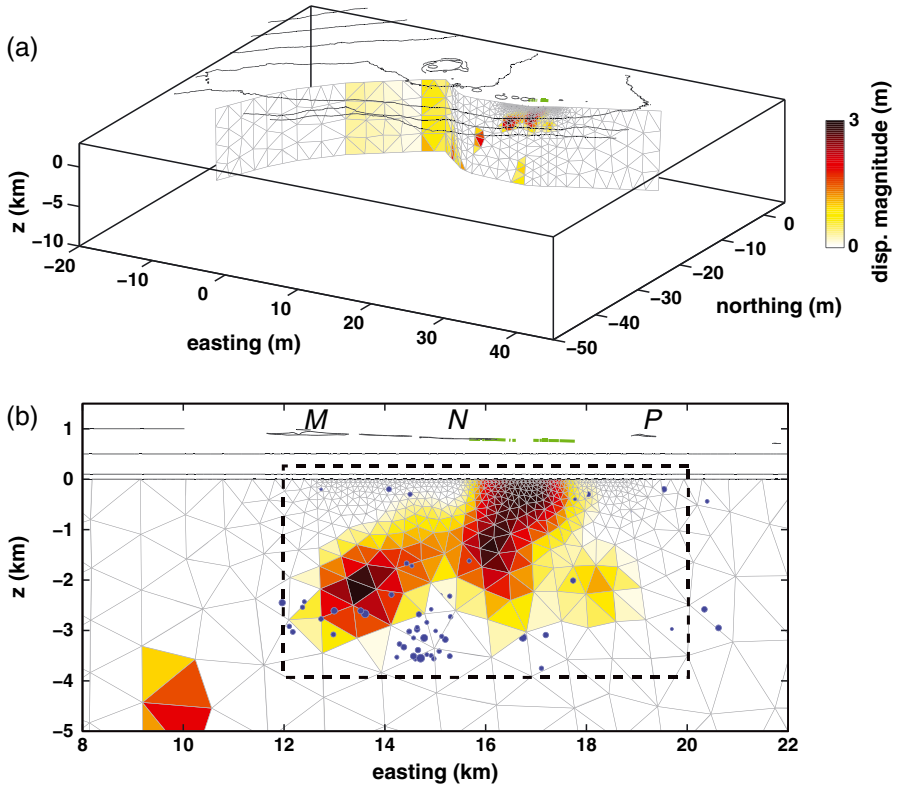

Figure 15. May 2011 rift-zone-only model dislocation magnitudes. (a) Perspective and (b) close-up side views. In Figure 15b, dashed box surrounding main dike shows the portion of the dike used to calculate dike volume; seismicity 5 March to 9 May (blue) is shown for the area within the dashed box in Figure 11a. *M*, *N*, and *P* indicate the Makaopuhi, Nāpau, and Pu`u `Ō`ō crater locations, respectively.

simple point (Mogi) source beneath Kīlauea Caldera using ascending and descending CSK data for 10–11 March and the three-component GPS displacements (Figures S10–S12), we find a volume decrease of 1.7 million cubic meters (MCM) for a source located at 1.7 km depth just NE of Halema`uma`u Crater, consistent with previous models of shallow magma accumulation and withdrawal beneath Kīlauea's summit during other time periods [e.g., *Cervelli and Miklius*, 2003; *Poland et al*., 2009; *Montgomery-Brown et al*., 2010]. The Pu`u `Ō`ō collapse volume has been estimated at 5.6 MCM, and the volume erupted from the fissure is approximately 2.7 MCM based on lava flow area and average flow thickness. Treating all volumes equally, this implies 7.3 MCM volume loss from the summit and Pu`u `Ō`ō sources and 18.3 MCM volume increase for the dike plus erupted lava at the end of the eruption. The erupted and intruded volume is therefore about 2.5 times larger than the source volume. This volume ratio is well within the range (1.24–4.33) found by *Rivalta and Segall* [2008] for realistic shear moduli and magma compressibilities of gas poor magmas, with the source and dike at the same depth and chamber compressibility. This suggests that no other magma sources are required beyond those beneath Pu`u `Ō`ō and Kīlauea's summit to explain the intrusion and eruption.

5.2. Comparison With Past Kilauea ERZ Intrusions/Eruptions

[36] Recent dike intrusions and eruptions along Kīlauea's ERZ show a variety of behaviors in terms of precursory summit deformation, whether an eruption occurred, and whether there was an associated slow-slip event on the décollement. Inflation of Kīlauea's summit, Pu`u `Ō`ō, and the east rift zone in the months before March 2011 (Figure 2), suggests that the Kamoamoa eruption resulted from overpressure of the magmatic system. The 1997 dike intrusion was similar to the 2011 event in terms of location and its onset was also marked by collapse of Pu`u `Ō`ō and deflation of Kīlauea's summit, however, there was no pre-eruption inflation in 1997. *Owen et al*. [2000a] found that the GPS displacements from the 1997 eruption required a summit volume loss of 1.5–2 MCM and a secondary volume decrease beneath Makaopuhi of 1.2 MCM, similar to the 1–1.5 MCM found by *Segall et al*. [2001] for a Makaopuhi source. Adding the volume loss from Pu`u `Ō`ō of 12.7 MCM [*Owen et al*., 2000a] to the Kīlauea summit and Makaopuhi source losses still results in a net deficit relative to the volume of the dike, 23 MCM plus the estimated erupted volume, 0.3 MCM [*Thornber et al*., 1997]. The 1997 Pu`u `O`o volume loss was more than twice that of the 2011 eruption, and the 2011 modeling did not require a source of volume loss beneath Makaopuhi. The volume loss for the Makaopuhi source of *Owen et al*. [2000a] was too shallow (0.6 km) and too large to have been missed by the 2011 InSAR data. The westernmost tail to our dike opening, however, does extend up-rift to beneath Makaopuhi, within 1 km of the modeled source location of *Owen et al*. [2000a], suggesting that, if a magma storage area does exist beneath Makaopuhi, it may have served as the starting point for the 2011 dike (even if it did not contribute volume to the dike).

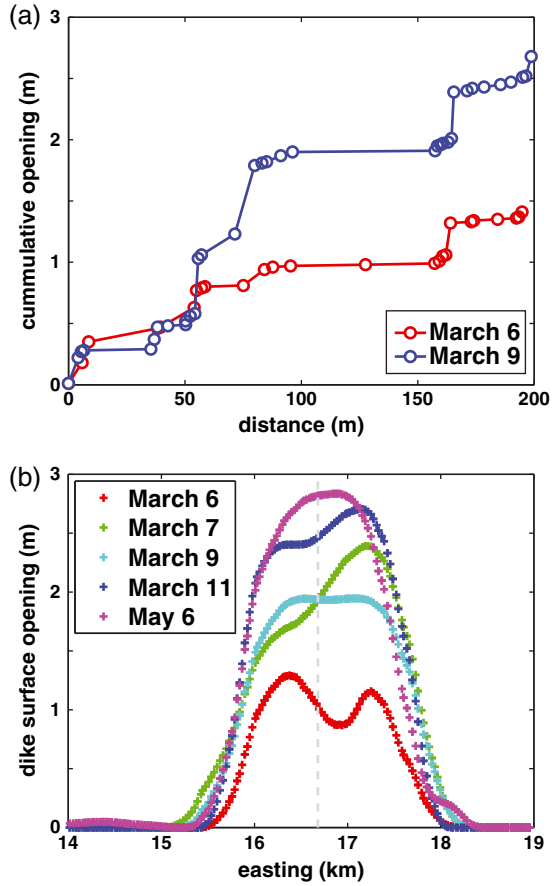

Figure 16. Comparison of observed and modeled surface opening. (a) Field observations of cumulative fracture opening along a profile across the center of the Kamoamoa eruption (between the two main east and west eruption segments). (b) Modeled surface opening. Dashed gray line indicates location of the measurements in Figure 16a.

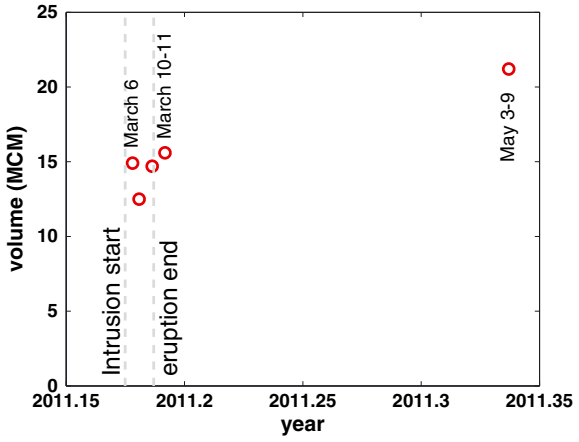

Figure 17. Dike volumes for the dashed box area shown in Figure 15b. Dashed lines mark the starting time of the dike intrusion and the end time of the fissure eruption.

[37] In September 1999, deformation and seismicity marked a dike intrusion just west of Mauna Ulu that was modeled by *Cervelli et al*. [2002] as a 3 km long by 2 km wide dike dipping steeply to the south based on GPS, tilt, and InSAR observations. The lack of inflation at Kīlauea's summit before the intrusion led *Cervelli et al*. [2002] to consider this to be a "passive" dike induced by deep rift extension, similar to the 1997 dike, with a volume of 3.3 MCM.

[38] The June 2007 dike intrusion had some significant differences from the 1997 and 1999 dikes. In the 3 years before the eruption, there was considerable inflation of Kīlauea's summit region that was interpreted as due to a surge in magma supply to the volcano [*Poland et al*., 2012]. A combination of GPS, tilt, and InSAR observations constrained the 2007 dike to two *en echelon* segments striking ENE, dipping steeply to the SSE from west of Mauna Ulu to just north of Makaopuhi, with a small eruption occurring from the down-rift end of the dike [*Montgomery-Brown et al*., 2010]. Similar to 1997, 1999, and 2011, the 2007 intrusion was marked by collapse of the Pu`u `Ō`ō crater floor (by 80 m) and deflation of Kīlauea's summit of 1.8 MCM from a source 1.5 km beneath the NE margin of Halema`uma`u Crater [*Montgomery-Brown et al*. [2010]. The dike volume modeled by *Montgomery-Brown et al*. [2010] was 16.6 MCM and the combined summit and Pu`u `Ō`ō volume loss was about 5.5 MCM, giving a ratio of dike volume to reservoir volume of 3.0, similar to the value of 2.5 that we found for the 2011 dike eruption. The 2007 diking event was also accompanied by slip on the décollement [*Brooks et al*., 2008; *Montgomery-Brown et al*., 2010] that followed the propagating dike intrusions and eventually spread westward on the detachment fault [*Montgomery-Brown et al*., 2011].

[39] There are interesting similarities and differences between these past intrusions and the 2011 Kamoamoa intrusion and eruption (Table 1). The 1997, 2007, and 2011 events had similar shallow volume losses from beneath Kīlauea's summit (~1.5–2 MCM). They also had similar dike intrusion plus eruption volumes (approximately 23, 17, and 18 MCM, for 1997, 2007, and 2011, respectively). The apparent similar volume loss from the shallow source beneath Kīlauea's summit for different intrusions suggests that a discrete volume from this source feeds the dike intrusion (i.e., in the case of these few samples the summit portion is relatively constant). The other common source for the dikes is Pu`u `Ō`ō, which may also supply similar volumes to intrusions. Compared with expected volume ratios (r_V) for source to dike for compressed magmas [*Rivalta and Segall*, 2008], the ratios found for the 2007 and 2011 intrusions ($r_V = 3.0$ and 2.5, respectively) do not require additional sources of magma feeding the dikes.

5.3. Relationship of Dike to Plumbing System

[40] The UAVSAR plus GPS model (Figure 15) shows evidence for most of the increase in dike volume occurring in the deeper portion of the 2011 intrusion that suggests post-diking deformation occurring in the months following the eruption, qualitatively similar to that observed for the 1997 intrusion [*Desmarais and Segall*, 2007]. What is not clear from these analyses is how the communication of magma from beneath Kīlauea's summit to the ERZ eruptive vents in and around Pu`u `Ō`ō, which respond rapidly during short-term deflation-inflation (DI) events [*Cervelli and Miklius*, 2003], relates to dike intrusion events. The dike growth model of *Segall et al*. [2001] conceives of a narrow, open conduit that feeds a growing semi-elliptical dike that

Table 1. Comparison of Intrusion, Erupted, and Source Volumes for Recent Diking Events

Year	Volume Change ($\times 10^6$ m^3, dense rock equivalent)					Volume Ratio (r_V)	Reference
	Kīlauea (loss)	Pu`u `Ō`ō (loss)	Makaopuhi (loss)	Lava	Dike		
1997	1.5–2	12.7	1.2	0.3	23	1.5	*Owen et al.* [2000a]
1999	–	–	–	–	3.3	–	*Cervelli et al.* [2002]
2007	1.8	3.7	–	–	16.6	3	*Montgomery-Brown et al.* [2010]
2011	1.7	5.6	–	2.7	15.6	2.5	This study

may or may not reach the surface. The shape of the dike opening that we find in our models is significantly different and more irregular, with the main limb of the dike deepening up-rift toward Kilauea, with a secondary source slightly down-rift suggesting a connection to beneath Pu`u `Ō`ō. The location of co-diking seismicity beneath the deep terminus of the up-rift limb of the dike suggests a broader feeding of the dike rather than a narrow (several meters) conduit [*Cervelli and Miklius*, 2003]. If the co-eruptive dike was formed by intrusion from both the Pu`u `Ō`ō, and summit directions via a connected conduit at roughly 3 km depth, then the continued opening of the central dike toward 3 km depth in the post-eruption interval could either be due to downward expansion of the shallower dike by accommodation to co-diking stress changes or upward migration through an additional entry point for conduit magma.

[41] We find a limiting depth of about 3 km for the co-diking intrusion (Figures 11 and 13) that could be consistent with the 3–5 km depth molten core to Kīlauea's ERZ as proposed by *Johnson* [1995]. The shape and size of the dike from our models suggest that the main branch stems from the level of the hypothesized Kilauea-ERZ conduit. In contrast, the down-rift projection to 2–2.5 km below the surface suggests a second link to the magmatic system beneath Pu`u `Ō`ō, where the dike intrusion was first observed. This may be from a depth intermediate between the 3+ km deep conduit and Pu`u `Ō`ō, at the surface (Figure 18).

[42] An additional aspect of the molten core model [*Johnson*, 1995] lies in the details of its heterogeneity. There has been a long-standing debate over whether there are separate magma reservoirs strung along the ERZ that might contribute to or modulate ERZ intrusions and eruptions. For example, *Swanson et al.* [1976] suggested a Makaopuhi source contributing to the large volume of magma in that area during the February 1969 eruption. In the 4 months prior to the 1969 eruption, there was significant inflation in the area around Makaopuhi, and significant seismicity was located there immediately prior to the eruption. *Owen et al.* [2000a] also modeled a very shallow point source beneath Makaopuhi—something we do not see evidence for in the 2011 dike model. This would have been evident in the InSAR data, especially the CSK ascending track data, where the trough of negative LOS that roughly follows the rift axis is what defines the trace (more or less) of the up-rift buried dike. In contrast a point source would add a circular subsidence bowl that is not apparent in the data. This up-rift trough is similar to the subsidence along the rift axis observed in InSAR data for the 2007 Father's Day intrusion [*Poland et al.*, 2008; *Sandwell et al.*, 2008; *Montgomery-Brown et al.*, 2009; *Jung et al.*, 2011].

[43] Examination of the GPS line-length change and InSAR time series (Figure 2a) shows that Kīlauea summit GPS expansion and increase in positive InSAR LOS occurred in the final 2 months of 2010, with overpressure of the magmatic plumbing system resulting in an "active" dike intrusion and eruption. As with past intrusions, the temporal response and volume changes at Kīlauea and Pu`u `Ō`ō show that the system is highly connected, with summit and Pu`u `Ō`ō inflation (Figures 2a and 2c) and rise in lava levels tracking together. This suggests that dike intrusion in the ERZ between Pu`u `Ō`ō and the summit occurs when the resulting overpressure reaches some critical level, with magma feeding

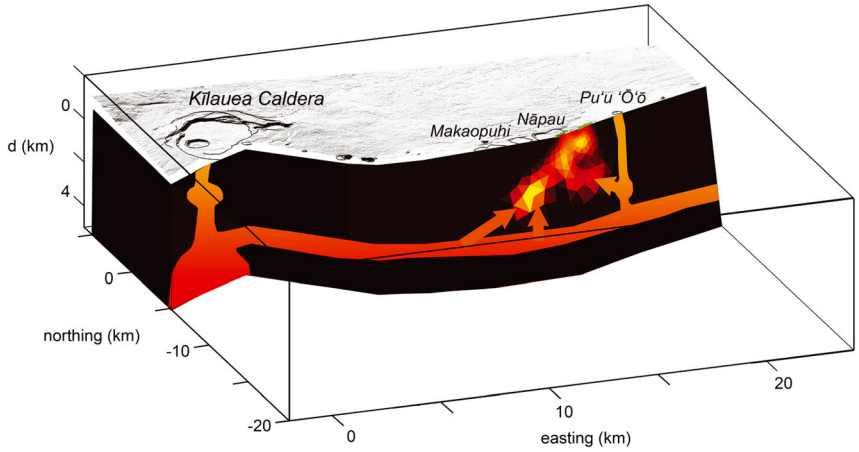

Figure 18. Conceptual model for the Kīlauea magmatic system related to the summit caldera source, the Pu`u `Ō`ō conduit, and the ERZ conduit thought to exist below 3 km depth. Model for 6 March is shown; red arrows show our interpretation of magma feeding the dike intrusion from the ERZ conduit from the up-rift limb of the dike and from the Pu`u `Ō`ō conduit in the down-rift direction.

the propagating dike from multiple directions (Figure 18). Following the Kamoamoa eruption, deflation at Kīlauea's summit quickly rebounded (Figure 2), with changes in eruptive vents near Pu`u `Ō`ō causing fluctuations in deformation throughout the remainder of 2011.

5.4. Data Limitations and Recommendations

[44] The InSAR data set available for the 5–9 March 2011 Kamoamoa eruption is one of the most detailed so far for a dike intrusion at Kīlauea and thus offers the potential to model the progression of the dike opening during and following emplacement. The temporal richness of the InSAR data set is somewhat complicated by the heterogeneity of radar wavelengths and look directions. Within the limitations of our modeling approach, it is evident that the spatial completeness of the L-band data (ALOS and UAVSAR) offers significant improvement in the displacement models. As is apparent for the 7 March model (Figures S5–S6), significant incoherence along the strike of the dike in the X-band data (CSK and TSX) leads to gaps in the dike due to reduced model constraints. While for all the models we show the weight of the GPS is a factor of 10 relative to the InSAR data, we have examined the effects of increased weighting on the GPS. For the 7 March model, increasing the weighting on the GPS (i.e., to a factor of 20 or greater) leads to increased opening at depth, which is necessary to better fit individual sparse GPS displacements, and of course increased misfit to the InSAR.

[45] Interpretations of the deeper portions of the models and areas where the model extends beyond the data must be made with caution (see checkerboard test, Figure S4). Recent advances in resolution-based scaling of dislocation patches and smoothing parameters in finite fault or dike modeling may improve shallow model detail while more realistically scaling deeper portions of the model [*Barnhart and Lohman*, 2010]. The broadness of deeper areas of opening and whether or not they are spurious (i.e., the opening area between 9 and 10 km easting and ~4 km depth in Figure 15) are open to interpretation and require additional sources of data, such as seismicity, for confirmation. Possible biases due to assumptions of an isotropic, elastic half-space with Poisson's ratio 0.25, although probably not significant in the upper few kilometers of the ERZ, may alter surface deformation Green's functions and the strengths and depths of inverted sources [*Masterlark et al*., 2012] and are likely biased in the deeper portions of the rift zone.

[46] Our analysis not only illustrates some of the limitations and shortcomings of current (and recently ended in the case of ALOS) satellite SAR missions for modeling dike processes but also shows the promise of having more frequent images with the seven SAR scenes acquired during and immediately following the eruption. To further advance our knowledge of dike intrusions, a finer temporal sampling (i.e., daily) from consistent imaging geometries is required. Additionally, our modeling shows the benefit of having an L-band radar for better coherence and model constraints in vegetated areas. Given the variations in surface deformation amplitudes present in volcanoes, X-band at short revisit times with tight orbital control to maintain small baselines would also be an alternative since for small ($<$10 cm) surface displacements. X-band generally has higher signal-to-noise ratio and would be more sensitive to the smaller deformation likely in the early phases of dike propagation.

6. Conclusions

[47] The InSAR and GPS observations of the 5–9 March 2011 Kamoamoa fissure eruption depict the growth of a dike from less than a day into the eruption to 2 months following its end. At the surface, our models show that dike opening along the eruptive fissures increased from nearly 1.5 m to over 2.8 m from the first day to immediately after the eruption, in agreement with field observations of surface fracturing. Surface dike opening ceased following the eruption, but the model ending in early May 2011 indicates increased opening in the deeper portions of the dike (less than 4 km depth) compared to the 10–11 March model. Checkerboard resolution tests show that dike opening is best resolved above 4 km depth, with trade-offs occurring between deeper dike opening and detachment slip. We find that the overall shape of the dike does not significantly change over the course of dike emplacement and post-diking deformation, but that the amount of opening, and therefore dike volume, does increase with time. Dike volumes increased from 15, to 16, to 21 MCM after the first day, end, and 2 months following the eruption, respectively. Dike opening was restricted to less than 3 km beneath the surface. The shape of the dike is distinctive, with a main limb plunging from the surface to 2–3 km depth to the WSW in the up-rift direction (i.e., toward Kīlauea's summit), and a lesser projection of dike opening extending in the down-rift direction toward Pu`u `Ō`ō at 2 km beneath the surface. We modeled deflation beneath Kīlauea's summit as a point source and found a depth beneath the surface of 1.7 km with a volume decrease of 1.7 MCM. Combined with estimates of Pu`u `Ō`ō volume loss (5.6 MCM) and dike (10–11 March model) plus erupted volume (18.3 MCM), these values yield a dike to source volume ratio of 2.5 that is in the range of expected volume change for compressible magma [*Rivalta and Segall*, 2008] and that does not require additional sources of magma. Inflation of Kīlauea's summit and east rift zone in the several months before the March 2011 eruption suggests that the Kamoamoa eruption resulted from overpressure of the volcano's magmatic system.

[48] **Acknowledgments.** The COSMO-SkyMed data were provided courtesy of the Italian Space Agency (ASI) under CSK AO Project ID 2270. The German Aerospace Center (DLR) TerraSAR-X data were courtesy of the Hawaii Supersite project GEO0875. ALOS PALSAR data were provided courtesy of the Japan Aerospace Exploration Agency (JAXA), Minestry of Economy, Trade and Industry (METI), which were distributed by the Earth Remote Sensing Data Analysis Center (ERSDAC). METI and JAXA retain ownership of the original ALOS PALSAR data. UAVSAR data were provided by the UAVSAR Project, JPL, with special thanks to Y. Zheng, Y. Lou, the radar operations personnel at JPL, and T. Moes and the flight operations personnel at NASA Dryden Flight Research Center. Maps in Figure 1 were generated using the public domain Generic Mapping Tools (GMT) software [*Wessel and Smith*, 1995]. Critical reviews from two anonymous reviewers and C. Wicks greatly improved the manuscript. Original TerraSAR-X data is copyright (2011) DLR. Original COSMO-SkyMed data copyright (2010, 2011). The research described in this paper was supported under contract with the National Aeronautics and Space Administration at the Jet Propulsion Laboratory, California Institute of Technology.

References

Barnhart, W. D., and R. B. Lohman (2010), Automated fault model discretization for inversions for coseismic slip distributions, *J. Geophys. Res.*, *115*, B10419, doi:10.1029/2010JB007545.

Brooks, B. A., J. Foster, D. Sandwell, C. J. Wolke, P. Okubo, M. Poland, and D. Mayer, Magmatically triggered slow slip at Kilauea Volcano, Hawaii (2008), *Science*, *321*, 1177, doi:10.1126/science.1159007.

Cayol, V., J. Dieterich, A. Okamura, and A. Miklius (2000), High magma storage rates before the 1983 eruption of Kilauea, Hawaii, *Science*, *288*(5475), 2343–2346, doi:10.1126/science.288.5475.2343.

Cervelli, P. F., and A. Miklius (2003), The shallow magmatic system of Kīlauea Volcano, *U.S. Geol. Survey Prof. Pap. 1676*, 149-164.

Cervelli, P., P. Segall, F. Amelung, H. Garbeil, C. Meertens, S. Owen, A. Miklius, and M. Lisowski (2002), The 12 September 1999 Upper East Rift Zone dike intrusion at Kilauea Volcano, Hawaii, *J. Geophys. Res.*, *107*(B7), 2150, doi:10.1029/2001JB000602.

Chen, C. W., and H. A. Zebker (2001), Two-dimensional phase unwrapping with use of statistical models for cost functions in non-linear optimization, *J. Opt. Soc. Am.*, *18*, 338–351.

Delaney, P. T., R. S. Fiske, A. Miklius, A. T. Okamura, and M. K. Sako (1990), Deep magma body beneath the summit and rift zones of Kilauea Volcano, *Hawaii, Science*, *247*, 1311-1316.

Desmarais, E., and P. Segall (2007), Transient deformation following the 30 January 1997 dike intrusion at Kilauea Volcano, Hawaii, *Bull. Volcanol.*, *69*(4), 353–363, doi:10.1007/s00445-006-0080-7.

Dieterich, J. (1988), Growth and persistence of Hawaiian volcanic rift zones, *J. Geophys. Res.*, *93*(B5), 4258–4270, doi:10.1029/JB093iB05p04258.

Fialko, Y., M. Simons, and D. Agnew (2001), The complete (3-D) surface displacement field in the epicentral area of the 1999 M_w7.1 Hector Mine earthquake, California, from space geodetic observations, *Geophys. Res. Lett.*, *28* (16), 3063–3066.

Fukuda, J., and K. M. Johnson (2010), Mixed linear–non-linear inversion of crustal deformation data: Bayesian inference of model, weighting and regularization parameters, *Geophys. J. Int. 181*, 1441–1458 doi:10.1111/j.1365-246X.2010.04564.x.

Goldstein, R. M., and C. L. Werner (1998), Radar interferogram filtering for geophysical applications, *Geophys. Res. Lett.*, *25*(21), 4035–4038, doi:10.1029/1998GL900033.

Goldstein, R. M., H. A. Zebker, and C. L. Werner (1988), Satellite radar interferometry: Two-dimensional phase unwrapping, *Radio Sci.*, *23*(4), 713–720, doi:10.1029/RS023i004p00713.

Gregorius, T. (1996), GIPSY-OASIS II: How It Works, Univ. of Newcastle upon Tyne, New Castle, U. K.

Hensley, S., K. Wheeler, G. Sadowy, et al. (2007), The UAVSAR instrument: Description and test plans, Proceedings *NASA Science Technology Conference 2007*, 10p.

Johnson, D. J., 1995, Molten core model for Hawaiian rift zones, *J. Volcanol. Geotherm. Res.*, *66*(1–4), 27–35, doi:10.1016/0377-0273(94)00066-P.

Jónsson, S., H. Zebker, P. Segall, and F. Amelung (2002), Fault slip distribution of the 1999 Mw 7.1 Hector Mine, California, earthquake, estimated from satellite radar and GPS measurements, *Bull. Seismol. Soc. Am.*, *92*, 1377–1389.

Jung, H. S., Z. Lu, J. S. Won, M. P. Poland, and A. Miklius, Mapping three-dimensional surface deformation by combining multiple aperture interferometry and conventional interferometry: Application to the June 2007 eruption of Kilauea Volcano, Hawaii (2011), *IEEE Geosci. Rem. Sens. Lett.*, *8*(1), 34–38, doi:10.1109/LGRS.2010.2051793.

Larson, K. M., M. Poland, and A. Miklius (2010), Volcano monitoring using GPS: Developing data analysis strategies based on the June 2007 Kīlauea Volcano intrusion and eruption, *J. Geophys. Res.*, *115*, B07406, doi:10.1029/2009JB007022.

Lohman, R. B., and M. Simons (2005), Some thoughts on the use of InSAR data to constrain models of surface deformation: Noise structure and data downsampling, *Geochem. Geophys. Geosyst.*, *6*, Q01007, doi:10.1029/2004GC000841.

Lundgren, P., and P. A. Rosen, Source model for the 2001 flank eruption of Mt. Etna volcano, *Geophys. Res. Lett.*, *30(7)*, 1388, doi:10.1029/2002GL016774, 2003.

Masterlark, T., K. L. Feigl, M. Haney, J. Stone, C. Thurber, and E. Ronchin (2012), Nonlinear estimation of geometric parameters in FEMs of volcano deformation: Integrating tomography models and geodetic data for Okmok volcano, Alaska, *J. Geophys. Res.*, *117*, B02407, doi:10.1029/2011JB008811.

Montgomery-Brown, E. K., P. Segall, and A. Miklius (2009), Kīlauea slow slip events: Identification source inversions, and relation to seismicity, *J. Geophys. Res.*, *114*, B00A03, doi:10.1029/2008JB006074.

Montgomery-Brown, E. K., D. K. Sinnett, M. Poland, P. Segall, T. Orr, H. Zebker, and A. Miklius (2010), Geodetic evidence for en echelon dike emplacement and concurrent slow slip during the June 2007 intrusion and eruption at Kīlauea volcano, Hawaii, *J. Geophys. Res.*, *115*, B07405, doi:10.1029/2009JB006658.

Montgomery-Brown, E. K., D. K. Sinnett, K. M. Larson, M. P. Poland, P. Segall, and A. Miklius (2011), Spatiotemporal evolution of dike opening and décollement slip at Kīlauea Volcano, Hawai`i, *J. Geophys. Res.*, *116*, B03401, doi:10.1029/2010JB007762.

Morgan, J. K. (2006), Volcanotectonic interactions between Mauna Loa and Kilauea: Insights from 2-D discrete element simulations, *J. Volcanol. Geotherm. Res.*, *151*, 109–131, doi:10.1016/j.jvolgeores.2005.07.025.

Morgan, J. K., G. F. Moore, D. J. Hills, and S. Leslie (2000), Overthrusting and sediment accretion along Kīlauea's mobile south flank, *Hawaii: Evidence for volcanic spreading from marine seismic reflection data, Geology*, *28*, 667–670.

Owen, S., P. Segall, J. Freymueller, A. Miklius, R. Denlinger, T. Arnadottir, M. Sako, and R. Burgmann (1995), Rapid deformation of the south flank of Kilauea volcano, Hawaii, *Science*, *267*, 1328–1332.

Owen, S., P. Segall, M. Lisowski, A. Miklius, R. Denlinger, and M. Sako (2000a), Rapid deformation of Kilauea Volcano: Global positioning system measurements between 1990 and 1996, *J. Geophys. Res.*, *105* (B8), 18,983–18,998, doi:10.1029/2000JB900109.

Owen, S., P. Segall, M. Lisowski, A. Miklius, M. Murray, M. Bevis, and J. Foster (2000b), January 30, 1997 eruptive event on Kilauea Volcano, Hawaii, as monitored by continuous GPS, *Geophys. Res. Lett.*, *27*(17), 2757–2760, doi:10.1029/1999GL008454.

Page, M. T., S. Custódio, R. J. Archuleta, and J. M. Carlson (2009) Constraining earthquake source inversions with GPS data: 1. Resolution-based removal of artifacts, *J. Geophys. Res.*, *114*, B01314, doi:10.1029/2007JB005449.

Pallister, J. S., W. A. McCausland, S. Jónsson, Z. Lu, H. M. Zahran, S. El Hadidy, A. Aburukbah, I. C. F. Stewart, P. R. Lundgren, R. A. White, and M. R. H. Moufti (2010), Broad accommodation of rift-related extension recorded by dyke intrusion in Saudi Arabia, *Nat. Geosci.*, *3*, 705–712, doi:10.1038/NGEO966.

Poland, M., A. Miklius, T. Orr, A. J. Sutton, C. Thornber, and D. Wilson (2008), New episodes of volcanism at Kīlauea Volcano, Hawaii, *EOS Trans. AGU*, *89*(5), 37, doi:10.1029/2008EO050001.

Poland, M. P., A. J. Sutton, and T. M. Gerlach (2009), Magma degassing triggered by static decompression at Kīlauea Volcano, Hawai`i, *Geophys. Res. Lett.*, *36*, L16306, doi:10.1029/2009GL039214.

Poland, M. P., A. Miklius, A. J. Sutton, and C. R. Thornber (2012), A mantle-driven surge in magma supply to Kīlauea Volcano during 2003–2007, *Nat. Geosci.*, *5*, 295–300, doi:10.1038/NGEO1426.

Rivalta, E., and P. Segall (2008), Magma compressibility and the missing source for some dike intrusions, *Geophys. Res. Lett.*, *35*, L04306, doi:10.1029/2007GL032521.

Rosen, P. A., S. Hensley, I. R. Joughin, F. K. Li, S. N. Madsen, E. Rodriguez, and R. M. Goldstein (2000), Synthetic aperture radar interferometry, *Proc. IEEE*, *88*, 333–382.

Rubin, A. M. (1993), Tensile fracture of rock at high confining pressure: Implications for dike propagation, *J. Geophys. Res.*, *98*(B9), 15,919–15,935.

Rubin, A. M., and D. D. Pollard (1987), Origins of blade-like dikes in volcanic rift zones, *U.S. Geol. Surv. Prof. Pap. 1350*, 1449–1470.

Ryan, M. P. (1988), The mechanics and three-dimensional internal structure of active magmatic systems: Kīlauea Volcano, Hawaii. *J. Geophys. Res. 93*, 4213–4248.

Sandwell, D. Y., D. Myer, R. Mellors, M. Shimada, B. Brooks, and J. Foster (2008), Accuracy and Resolution of ALOS Interferometry: Vector deformation maps of the Father's Day intrusion at Kilauea, *IEEE Trans. Geosci. Rem. Sens.*, *46* (11), 3524–3534.

Segall, P., P. Cervelli, S. Owen, M. Lisowski, and A. Miklius (2001), Constraints on dike propagation from continuous GPS measurements, *J. Geophys. Res.*, *106* (B9), 19,301–19,317.

Swanson, D. A., D. B. Jackson, R. Y. Koyanagi, and T. L. Wright (1976), The February 1969 east rift eruption of Kilauea Volcano, Hawaii, *U. S. Geol. Surv. Prof. Pap. 891*, 1–30.

Syracuse, E. M., C. H. Thurber, C. J. Wolfe, P. G. Okubo, J. H. Foster, and B. A. Brooks (2010), High-resolution locations of triggered earthquakes and tomographic imaging of Kilauea Volcano's south flank, *J. Geophys. Res.*, *115*, B10310, doi:10.1029/2010JB007554.

Thornber, C., D. Sherrod, C. Helliker, J. J. Kauahikaua, F. Trusdell, M. Lisowski, and d P. Okubo (1997), Kilauea's ongoing eruption: Napau Crater revisited after 14 years, *Eos Trans., AGU*, *78*, 329.

Wessel, P., and W. H. F. Smith (1995), New version of the generic mapping tools released, *Eos Trans. AGU*, *76*, 329.

Wright, T. J., C. Ebinger, J. Biggs, A. Ayele, G. Yirgu, D. Keir, and A. Stork, Magma-maintained rift segmentation at continental rupture in the 2005 Afar dyking episode (2006), *Nature*, *442*, 291–294, doi:10.1038/nature04978.

Yun, S., P. Segall, and H. Zebker (2006), Constraints on magma chamber geometry at Sierra Negra Volcano, Galapagos Islands, based on InSAR observations, *J. Volcanol. Geotherm. Res.*, *150* (1–3), 232–243.

Zumberge, J. F., M. B. Heflin, D. C. Jefferson, M. M. Watkins, and F. H. Webb (1997), Precise point positioning for the efficient and robust analysis of GPS data from large networks, *J. Geophys. Res.*, *102*(B3), 5005–5017, doi:10.1029/96JB03860.